

DTIC FILE COPY

1

AD-A218 273

APPLICATIONS OF MICROWAVE
RADIOMETRIC MEASUREMENTS TO INFER
TROPICAL CYCLONE INTENSITY AND STRENGTH

DTIC
ELECTE
FEB 22 1990
S D
D

Don Kenneth Rhudy, B.S.

DISTRIBUTION STATEMENT A

Approved for public release
Distribution Unlimited

A Digest Presented to the Faculty of the Graduate
School of Saint Louis University in Partial
Fulfillment of the Requirements for the
Degree of Master of Science (Research)

1989

90 02 21 084

REPORT DOCUMENTATION PAGE

Form Approved
OMB No. 0704-0188

1a. REPORT SECURITY CLASSIFICATION UNCLASSIFIED			1b. RESTRICTIVE MARKINGS NONE		
2a. SECURITY CLASSIFICATION AUTHORITY			3. DISTRIBUTION/AVAILABILITY OF REPORT APPROVED FOR PUBLIC RELEASE; DISTRIBUTION UNLIMITED.		
2b. DECLASSIFICATION/DOWNGRADING SCHEDULE					
4. PERFORMING ORGANIZATION REPORT NUMBER(S)			5. MONITORING ORGANIZATION REPORT NUMBER(S) AFIT/CI/CIA- 89-063		
6a. NAME OF PERFORMING ORGANIZATION AFIT STUDENT AT SAINT LOUIS UNIVERSITY		6b. OFFICE SYMBOL (If applicable)	7a. NAME OF MONITORING ORGANIZATION AFIT/CIA		
6c. ADDRESS (City, State, and ZIP Code)			7b. ADDRESS (City, State, and ZIP Code) Wright-Patterson AFB OH 45433-6583		
8a. NAME OF FUNDING/SPONSORING ORGANIZATION		8b. OFFICE SYMBOL (If applicable)	9. PROCUREMENT INSTRUMENT IDENTIFICATION NUMBER		
8c. ADDRESS (City, State, and ZIP Code)			10. SOURCE OF FUNDING NUMBERS		
			PROGRAM ELEMENT NO.	PROJECT NO.	TASK NO.
			WORK UNIT ACCESSION NO.		
11. TITLE (Include Security Classification) (UNCLASSIFIED) Applications of Microwave Radiometric Measurements to Infer Tropical Cyclone Intensity and Strength					
12. PERSONAL AUTHOR(S) Don Kenneth Rhudy					
13a. TYPE OF REPORT THESIS/DISSERTATION		13b. TIME COVERED FROM _____ TO _____		14. DATE OF REPORT (Year, Month, Day) 1989	
				15. PAGE COUNT 91	
16. SUPPLEMENTARY NOTATION APPROVED FOR PUBLIC RELEASE IAW AFR 190-1 ERNEST A. HAYGOOD, 1st Lt, USAF Executive Officer, Civilian Institution Programs					
17. COSATI CODES			18. SUBJECT TERMS (Continue on reverse if necessary and identify by block number)		
FIELD	GROUP	SUB-GROUP			
19. ABSTRACT (Continue on reverse if necessary and identify by block number)					
20. DISTRIBUTION/AVAILABILITY OF ABSTRACT <input checked="" type="checkbox"/> UNCLASSIFIED/UNLIMITED <input type="checkbox"/> SAME AS RPT. <input type="checkbox"/> DTIC USERS					
21. ABSTRACT SECURITY CLASSIFICATION UNCLASSIFIED					
22a. NAME OF RESPONSIBLE INDIVIDUAL ERNEST A. HAYGOOD, 1st Lt, USAF			22b. TELEPHONE (Include Area Code) (513) 255-2259		22c. OFFICE SYMBOL AFIT/CI

DIGEST

1
Microwave radiometric data from the DMSP Special Sensor Microwave Imager (SSM/I) are available in the form of Environmental Data Records (EDR's) and Sensor Data Records (SDR's). The EDR's provide meteorological parameters such as rain rates and surface wind speeds over the oceans, while the SDR's provide the measured brightness temperatures (TB's). In the following study, the EDR's were used to compute latent heat released (LHR) in tropical cyclones. The TB's at 85 GHz were used to diagnose the current intensity of the tropical cyclone. R. J. S.

The rain rates offer the unique opportunity to study the rainband structure of tropical cyclones. The asymmetry associated with tropical cyclones was very apparent in this study.

Despite spatial and temporal problems, the SSM/I derived wind speeds verified well with those measured conventionally under rain-free conditions. However, in the presence of rain the SSM/I showed serious problems in accurately determining wind speeds. In fact, its inability to accurately measure wind speeds near the cyclone

center, because of heavy rain, casts serious doubts on its usefulness in this regard.

The use of 85 GHz vertically polarized (TB) data shows promise in its ability to determine the current intensity (in terms of maximum surface winds), as well as the 24 hour intensity of a cyclone. The differences between the average 85 GHz TB near the core of the cyclone and the corresponding TB of the surrounding environment was well correlated with the intensity. Furthermore, the 85 GHz vertically polarized TB's revealed the eye as a warm point in the temperature field. The colder temperatures surrounding the eye were the result of scattering caused by ice hydrometeors associated with the heavy convection. This suggests a potential use for this TB data in the understanding and prediction of the intensity of tropical cyclones.



APPLICATIONS OF MICROWAVE
RADIOMETRIC MEASUREMENTS TO INFER
TROPICAL CYCLONE INTENSITY AND STRENGTH

Don Kenneth Rhudy, B.S.

A Thesis Presented to the Faculty of the Graduate
School of Saint Louis University in Partial
Fulfillment of the Requirements for the
Degree of Master of Science (Research)

1989

COMMITTEE IN CHARGE OF CANDIDACY:

Professor Gandikota V. Rao,
Chairperson and Advisor

Assistant Professor Lawrence Coy

Associate Professor James T. Moore

ACKNOWLEDGMENTS

I would like to express my appreciation to several people who helped in the completion of this research. Professor Gandikota V. Rao, whose guidance and support made this research possible. Appreciation also goes to Dr. James T. Moore and Dr. Lawrence Coy for their thoughts and comments. A special thanks is extended to Mr. Gerald Felde of the Air Force Geophysics Lab who provided all of the SSM/I data used in this research. Mr. Ken Hill kept me informed of the tropical cyclone activity by monitoring the typhoon bulletins at HQ Air Weather Service. Mr. Mark Baricevic of the St. Louis University Computer Center assisted in the processing of the SSM/I data tapes. And finally to my wife Martha, who was always there when I needed her advice.

TABLE OF CONTENTS

	Page
Chapter 1. Introduction.....	1
Chapter 2. Review of Related Literature.....	3
Chapter 3. Radiative Transfer Theory at SSM/I Frequencies	
3a. DMSP SSM/I instrument description...	7
3b. Definition of brightness temperatures.....	11
3c. Effects of the atmosphere on SSM/I frequencies.....	13
3d. Changes in surface emission.....	20
Chapter 4. SSM/I Derived Rain Rates	
4a. Latent heat release.....	24
4b. Data analysis.....	26
4c. Results of LHR calculations.....	28
4d. Observations of rainband structure..	33
Chapter 5. SSM/I Derived Wind Speeds	
5a. Data analysis.....	39
5b. Results.....	43
Chapter 6. 85 GHz Brightness Temperatures	
6a. Background and channel determination.....	52
6b. Data analysis and results.....	60
6c. 85 GHz TB's as a forecasting parameter of cyclone intensity.....	68
6d. Detection of a tropical cyclone eye.....	73
Chapter 7. Conclusions.....	83
References.....	87
Biography of the Author.....	91

LIST OF TABLES

	Page
Table 4.1 Results of LHR ($\times 10^{14}$ W), average rain rate (mm hr^{-1}), and PIP calculations.....	29
Table 4.2 Mean rain rate comparisons for mature cyclones (mm hr^{-1}).....	30
Table 5.1 Results of wind speed study.....	44

LIST OF ILLUSTRATIONS

	Page
Figure 3.1. Scan geometry for the DMSP SSM/I (Hollinger et al., 1987).....	8
Figure 3.2. SSM/I scan geometry including swath width, footprint sampling locations, and integrated fields of view (Spencer et al., 1988) ..	10
Figure 3.3. Calculated oxygen absorption for sea-level conditions (Ulaby et al., 1981).....	14
Figure 3.4. Extinction coefficients for oxygen and water vapor at $T=293^{\circ}\text{K}$ and $P=1000\text{ mb}$ (Olson, 1987).....	15
Figure 3.5. (a) Mie volume scattering coefficients. (b) Volume absorption coefficients. (c) Single scattering albedos. All are for a Marshall-Palmer precipitation size distribution of liquid and ice hydrometeors. Data is not included for the 22.235 GHz channel (Spencer et al., 1988).....	17
Figure 3.6. Brightness temperature - rain rate relationships at 18, 37, and 85.6 GHz. Results were calculated using the radiative transfer model of Wu and Weinman (1984). The vertical distribution of hydrometeors was based upon averaged radar results and assume ice hydrometeors above and liquid hydrometeors below the freezing level (Spencer et al., 1987).....	19
Figure 3.7. Brightness temperatures as a function of frequency, polarization (V = vertical, H = horizontal), and wind speed (Hollinger et al., 1987).....	23
Figure 4.1. Scatter plot of cyclone intensity versus latent heat release for 23 cases. Equation of best fit line, number of cases, and correlation coefficient are shown in the upper left hand corner.....	32
Figure 4.2. Plot of SSM/I rain rates for Typhoon Dinah.....	35
Figure 4.3. As in Fig. 4.2 except for Typhoon Holly.....	36

Figure 4.4. As in Fig. 4.2 except for Typhoon Wynne.....	37
Figure 5.1. Scatter plot of SSM/I derived wind speeds versus "truth" data along with linear regression line.....	45
Figure 5.2. As in Fig. 5.1 except the temporal criteria is ± 1 hour and a nonlinear regression line is used.....	47
Figure 5.3. As in Fig. 5.1 except "truth" data is only for stations reporting precipitation.....	49
Figure 5.4. As in Fig. 5.3 except the temporal criteria is ± 1 hour.....	50
Figure 6.1. Temporal changes of mean equivalent blackbody temperatures and maximum winds of Typhoons Holly (Sept 1970) and Billy (Aug 1970). The temperature scale is inverted to show the lower temperature at the top of the graph (Gentry et al., 1980).....	53
Figure 6.2. Central pressure versus maximum brightness temperature anomaly within 2° latitude of the cyclone center (Kidder et al., 1978).....	55
Figure 6.3. Brightness temperature calculations for 92 GHz. Values adjacent to curves indicate the thickness of the ice layer. The assumed freezing level is 5 km (Wilheit et al., 1982)....	56
Figure 6.4. West to east cross section through Typhoon Dinah (25 Aug 1987 @ 0935 UTC). Distance in Km from the center of the cyclone are depicted on the x-axis. Dashed line represents TB's, while solid line represents rain rates.....	57
Figure 6.5. As in Fig. 6.4 except for Typhoon Cary (14 Aug 87 @ 2120 UTC).....	58
Figure 6.6. Empirical relationship between the current intensity number (CI), the maximum mean wind speeds (MWS), and the minimum sea level pressure (MSLP) in tropical cyclones (Dvorak, 1984).....	61

Figure 6.7. Scatter plot of tropical cyclone maximum wind speeds versus 85 GHz vertically polarized brightness temperature difference for the 3x3° inner box case.....	63
Figure 6.8. As in Fig. 6.7 except for the 2x2° inner box case.....	64
Figure 6.9. As in Fig. 6.7 except for the 4x4° inner box case.....	65
Figure 6.10. Scatter plot of 24 hour cyclone maximum wind speeds versus 85 GHz vertically polarized brightness temperature difference for the 3x3° inner box case.....	70
Figure 6.11. As in Fig. 6.10 except for the 2x2° inner box case.....	71
Figure 6.12. As in Fig. 6.10 except for the 4x4° inner box case.....	72
Figure 6.13. North-south cross section of TB's for Typhoon Dinah. Distance in Km from the center of the cyclone are depicted on the x-axis.....	75
Figure 6.14. As in Fig. 6.13 except this is a west-east cross section.....	76
Figure 6.15. As in Fig. 6.13 except for Typhoon Holly.....	78
Figure 6.16. As in Fig. 6.14 except for Typhoon Holly.....	79
Figure 6.17. As in Fig. 6.13 except for Typhoon Wynne.....	80
Figure 6.18. As in Fig. 6.14 except for Typhoon Wynne.....	81

1. INTRODUCTION

In October 1987, the U.S. Air Force aerial reconnaissance of tropical cyclones in the western Pacific was discontinued for budgetary reasons. Increased reliance is being placed on obtaining information from satellite sensors, such as the new Special Sensor Microwave Imager (SSM/I). This sensor is on-board the Defense Meteorological Satellite Program (DMSP) spacecraft which was launched on 19 June 1987. With this instrument measuring emitted microwave energy at four different frequencies and determining such parameters as wind speeds and rain rates over the oceans, it is possible to replace some of the data no longer available because of the shut-down of the reconnaissance aircraft.

This research aims to develop techniques to determine the intensity and strength of tropical cyclones using the SSM/I data. In particular:

- 1) The SSM/I rain rates, for a total of 23 SSM/I passes covering various tropical cyclones, will be used to calculate the latent heat release (LHR) associated with the convection and precipitation processes of the tropical cyclones. It is hypothesized that the intensity of the

cyclones as measured by the Dvorak technique, will be well correlated with the LHR.

2) The 85 GHz vertically polarized brightness temperatures (TB's) show significant variation over the tropical cyclone. It is hypothesized that the extremely cold TB's represent deep convection, and the structure of the cyclones' rainbands can be studied with these TB's.

3) It is further hypothesized that based on the revised coefficients, the SSM/I derived wind speeds correlate well with land/ship winds. The SSM/I derived wind speeds will be examined in rain and non-rain conditions. This will be important in determining whether the SSM/I wind speeds will be accurate within tropical cyclones.

4) The 85 GHz vertically polarized TB's will be plotted in an area surrounding the cyclone center to test whether the cyclone intensity can be inferred from the temporal and spatial variation of these temperatures. It is hypothesized that these TB's can be used to forecast future cyclone intensity. Similarly, the feasibility of using these TB's to pinpoint the eye of a tropical cyclone, even if covered by a thin layer of cirrus, will be examined.

2. REVIEW OF RELATED LITERATURE

Measurements of rainfall, wind, and intensity of tropical cyclones have been made for the past 50 years using meteorological sensors based on land, ships, and aircraft; conventional weather radar and satellite imagery. However, all of these measurements have certain drawbacks, the most serious of which is limited spatial coverage. Early satellite coverage (infrared and visible) was an improvement and overcame the lack of spatial coverage, but cloud cover prevented the visible and infrared wavelengths from penetrating the thick upper cirrus cloud layer of the tropical cyclones. Only in the past 15 years has it been possible for satellites to measure the microwave emissions from the surface layers through the thick cloud cover of the cyclone.

The early work in microwave radiometry was focused on the determination of surface wind speeds and rain rates over oceans. Norberg et al. (1971) used aircraft observations to verify the existence of a linear relationship between the increase in microwave emission over the ocean and an increase in wind speeds ($>7 \text{ m s}^{-1}$). They concluded that this increase in microwave emission was mainly due

to foam and spray, caused by increasing wave action, associated with an increase in wind speed. The increase in foam causes an increase in the overall emissivity of the oceanic background. This will lead to an increase in measured brightness temperatures (TB's).

Allison et al. (1974) made the first study of tropical cyclone structure using emitted microwave radiance measurements. They used data from the Electrically Scanning Microwave Radiometer (ESMR) launched aboard the Nimbus 5 spacecraft on 11 December 1972. The ESMR measured earth and atmospheric radiation with a frequency of 19.35 GHz. Allison et al. (1974) showed that this type of microwave data could be used to delineate rainfall areas and also provide, semi-quantitatively, rain rates within a tropical cyclone. Wilheit et al. (1977) showed that TB's measured at 19.35 GHz could be used to interpret the rainband structure of a tropical cyclone with an accuracy of about a factor of two for rain rates over the range of $0-25 \text{ mm hr}^{-1}$. Lovejoy and Austin (1980) estimated an accuracy of only 70% when measuring rain rates using satellite-borne microwave radiometry. The lack of accuracy was due to the unknown amount of cloud water content and

the thickness of the rain layer, and the inability to specify these quantities in radiative transfer models.

Despite these drawbacks it appears the structure and intensity of tropical storms can be inferred from emitted microwave radiances. Adler and Rodgers (1977) and Rodgers and Adler (1981) used ESMR data from 70 satellite passes covering 21 tropical cyclones in the north Pacific to calculate rain rates and resultant latent heat release. They concluded that the microwave data was useful in determining the rainfall characteristics of tropical cyclones and may be helpful as a tool to monitor, as well as to predict, the intensity of tropical cyclones. The ESMR derived total cyclone rain rates were in good agreement with previous estimates, which were based on moisture budget computations.

One of the goals of this research is to use the TB's from the 85 GHz vertically polarized channel and infer the cyclone intensity. Kidder et al. (1978) used the 55.45 GHz channel of the Scanning Microwave Spectrometer to estimate the central pressure and maximum winds in tropical cyclones. They found a strong relationship between

the brightness temperature anomaly within 2° latitude of the cyclone center and its central pressure.

The idea that the SSM/I 85 GHz channel TB's will be useful to predict cyclone intensity has been documented by the work of several authors. Gentry et al. (1980) found a strong correlation between the measured equivalent blackbody temperatures of cloud tops near the core of a tropical cyclone and its intensity. Wilheit et al. (1982) as well as Wu and Weinman (1984) have both indicated that the SSM/I 85 GHz channel would be useful for this purpose because of its interaction with ice crystals, and the fact that the 85 GHz TB's will almost linearly decrease with increasing rain rates.

3. RADIATIVE TRANSFER THEORY AT SSM/I FREQUENCIES

a. DMSP SSM/I instrument description

The SSM/I is one of several sensing systems which operate on-board the DMSP spacecraft. The DMSP spacecraft orbits the earth in a circular sun-synchronous near-polar orbit. Its orbit altitude is 833 km with an inclination of 98.8 degrees and an orbital period of 102 minutes. This type of orbit produces 14.1 full revolutions per day, with an 0612 local time equatorial crossing. As the spacecraft crosses the equator at 0612 local time it is going from south to north, conventionally called an ascending orbit.

The SSM/I is a seven channel, four frequency, linearly polarized, passive microwave system. It measures radiation emitted and scattered by the earth's surface and atmosphere at 19.35, 22.235, 37.0, and 85.5 GHz (1.55, 1.35, 0.81, and 0.35 cm respectively). Fig. 3.1 shows the SSM/I scan geometry. The SSM/I scans the earth at a 45° angle in the aft direction. Its active scan angle is 102° which produces a 1394 km swath width. The SSM/I rotates at a rate of 31.6 rpm while the DMSP spacecraft orbits the earth at 6.58 km s^{-1} . This produces a 12.5 km separation between successive

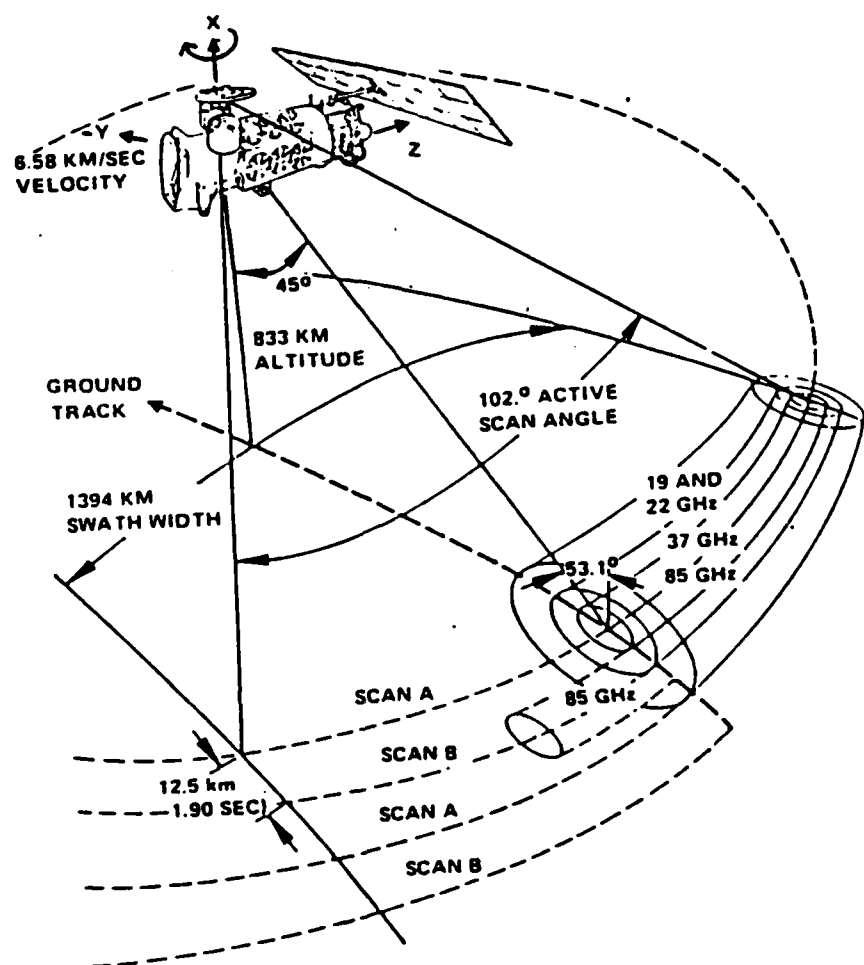


Figure 3.1. Scan geometry for the DMSP SSM/I (Hollinger et al., 1987).

scans. On each scan, 128 uniformly spaced samples of radiation at 85.5 GHz are taken producing a separation of 12.5 km between samples. On every other scan, 64 uniformly spaced samples of radiation at the remaining frequencies are taken, which produces a separation of 25 km. Listed below are the SSM/I footprint (projection of the 3-dB beamwidth on the earth's surface) dimensions depicted in Fig. 3.2:

19.35 GHz	69x43 km
22.235 GHz	50x40 km
37.0 GHz	37x28 km
85.5 GHz	15x13 km

In this study two sets of data from the SSM/I are used. The first are Sensor Data Records (SDR's). These consist of TB's at each SSM/I pixel point. These TB's are obtained from the antenna temperature (TA). The TA is the temperature sensed by the radiometer. This value includes contributions from sources other than the earth scene for which we're interested in obtaining a TB. An antenna pattern correction is then applied to arrive at a TB. Hollinger et al. (1987) give a complete description of this antenna pattern

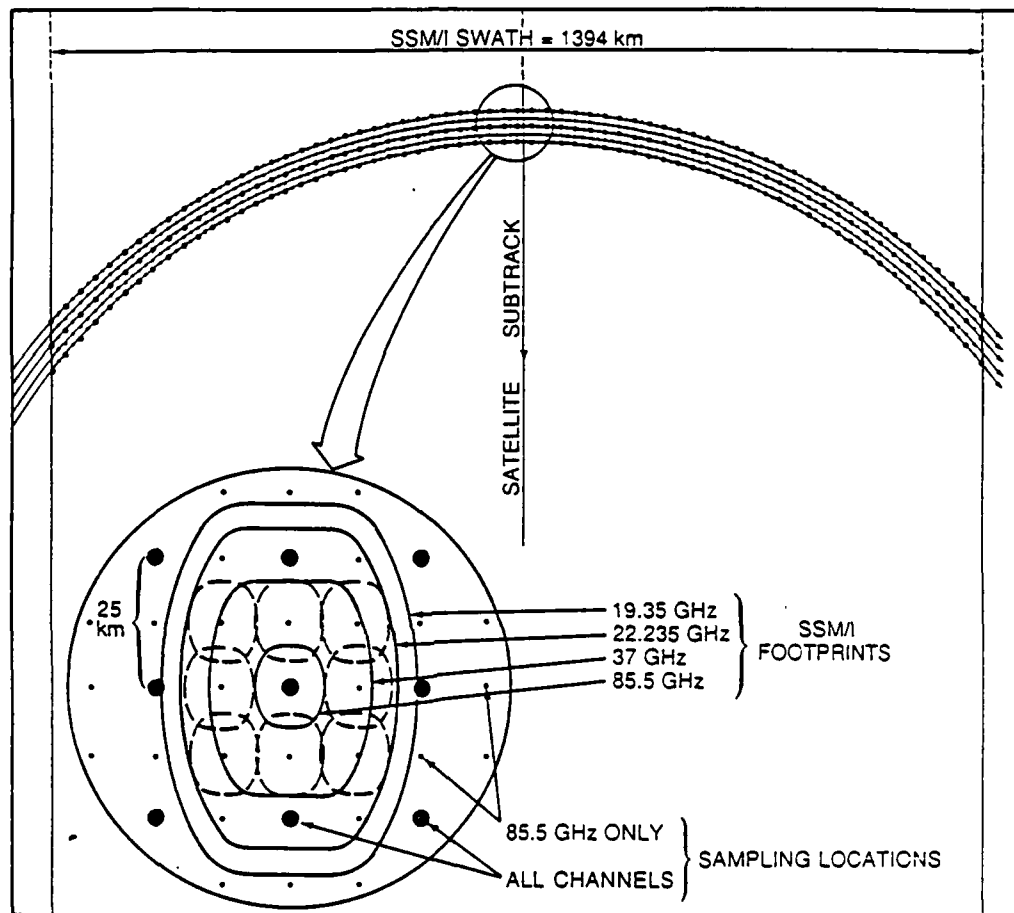


Figure 3.2. SSM/I scan geometry including swath width, footprint sampling locations, and integrated fields of view (Spencer et al., 1988).

correction.

The second set of data are the actual environmental parameters (wind speed, rainfall rates, etc.) calculated at each pixel from the TB's. These are called Environmental Data Records (EDR's). Once again refer to Hollinger et al. (1987) for a complete explanation of how the EDR's are calculated.

b. Definition of brightness temperature

When dealing with microwave remote sensing, the term equivalent brightness temperature is used. At a given intensity of thermal emission, B_v , the brightness temperature is the thermodynamic temperature a blackbody would have if it emitted at the same intensity.

By definition, a blackbody radiates uniformly in all directions with an intensity given by Planck's law

$$B_v = \frac{2hv^3}{c^2(e^{\frac{hv}{KT}} - 1)} \quad (1)$$

If we set $v = 37$ GHz and use the following values;

$$h = 6.6262 \times 10^{-27} \text{ erg sec} \quad (\text{Planck's constant})$$

$$k = 1.3806 \times 10^{-16} \text{ erg day}^{-1} \quad (\text{Boltzman constant})$$

$$c = 3 \times 10^8 \text{ m sec}^{-1}$$

$$T = 280^\circ \text{K}$$

we see that $\frac{h\nu}{KT} \ll 1$, and in fact this holds for most of the microwave region used for meteorological purposes.

If we let $x = \frac{h\nu}{KT}$, then through Taylor series expansion

$$e^x = 1 + x + \frac{x^2}{2!} + \dots \quad (2)$$

therefore

$$e^x - 1 \approx x \quad (3)$$

With this, the Planck function can be rewritten as

$$B_\nu = \frac{2h\nu^3}{c^2 x} = \frac{2K\nu^2 T}{c^2} \quad (4)$$

Because most bodies do not behave as a perfect blackbody, we use the brightness temperature, TB, so that

$$B_\nu' = \frac{2K\nu^2 TB}{c^2} \quad (5)$$

Where B_ν' is used to denote a non-blackbody.

By definition the emissivity of a nonblackbody is given by

$$\epsilon = \frac{B'_v}{B_v} \quad (6)$$

therefore

$$\epsilon = \frac{TB}{T} \text{ or } TB = \epsilon T \quad (7)$$

So we see that the brightness temperature of a material will always be less than or equal to its physical temperature. We now turn our attention to what constituents in the atmosphere affect the microwave emissions as measured by a space-borne radiometer.

c. Effects of the atmosphere on SSM/I frequencies

Molecular oxygen and water vapor are the only significant gaseous absorbers of microwave radiation in the atmosphere. Scattering is not significant for either of these two molecules. Fig. 3.3 shows that molecular oxygen has major absorbing peaks near 60 GHz and 118.75 GHz. Water vapor has a major absorption band at 22.235 GHz. As seen in Fig. 3.4 the amount of absorption varies in proportion to the relative humidity (concentration of water vapor). Olson (1986) showed that at low frequencies (19 and 22 GHz) the extinction by water vapor, at relative humidities approaching 100%, can be equivalent to rain at a rainfall rate of up to 4 mm hr^{-1} . So he concluded

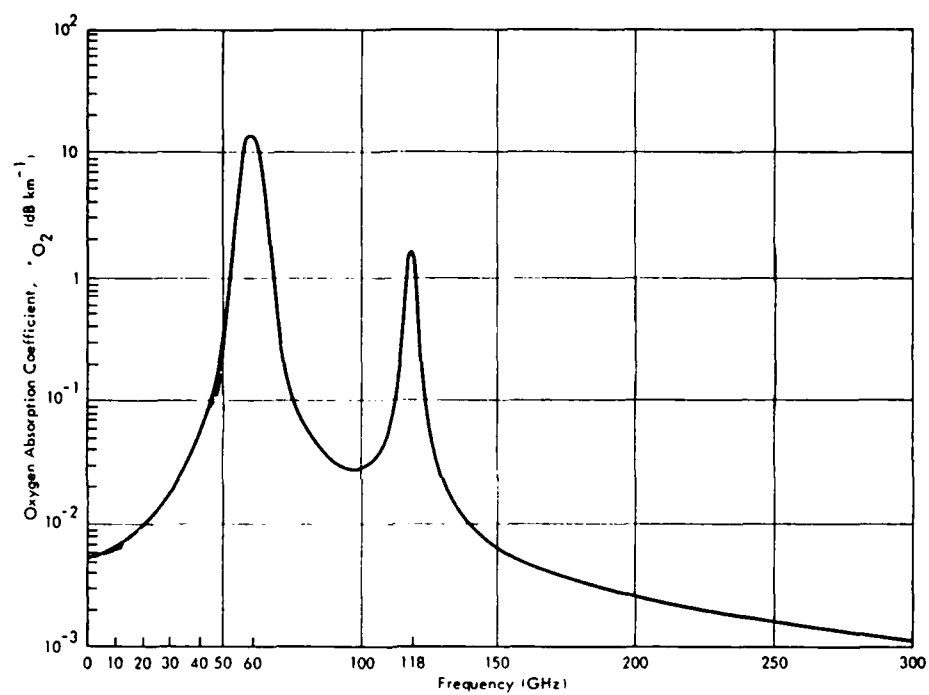


Figure 3.3. Calculated oxygen absorption for sea-level conditions (Ulaby et al., 1981).

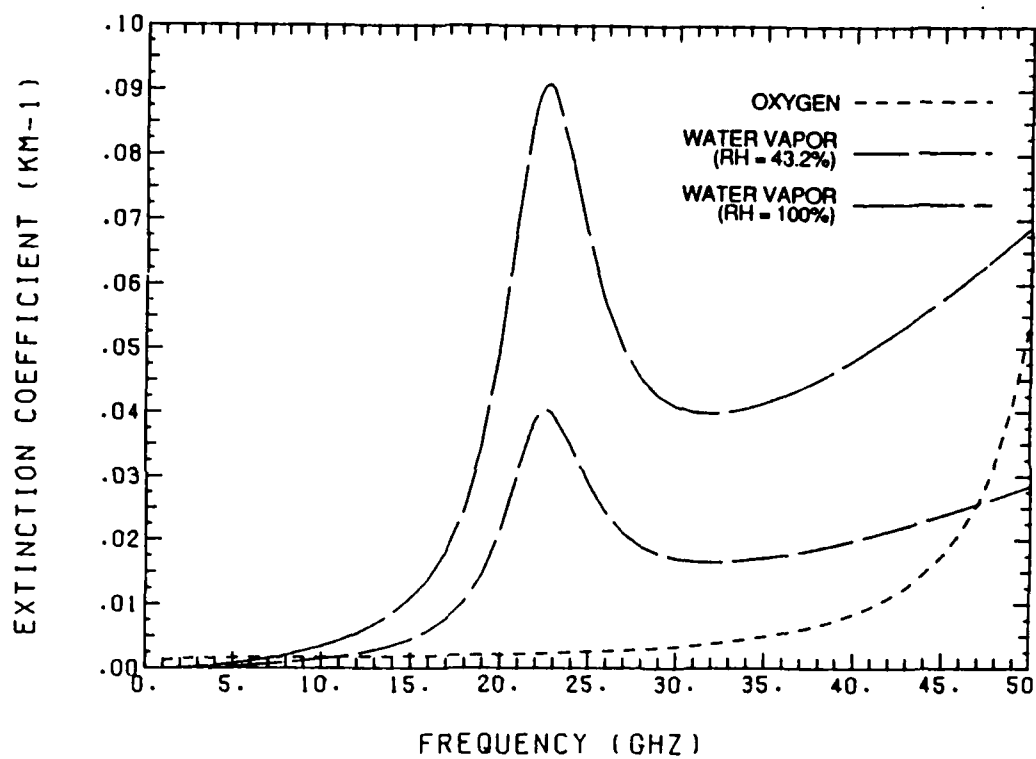


Figure 3.4. Extinction coefficients for oxygen and water vapor at $T=293^{\circ}\text{K}$ and $P=1000\text{ mb}$ (Olson, 1987).

that the effects of absorption by water vapor must be taken into consideration, especially near precipitating clouds where the level of water vapor does approach saturation.

Raindrops (liquid hydrometeors) with radii greater than $100\mu\text{m}$ but less than 5 mm have a greater effect on microwave emission. Olson (1986) showed that the radiative extinction (absorption and scattering) by rain is significant and increases with increasing frequency (Fig. 3.5). For cloud droplets ($r < 100\mu\text{m}$) the effects of scattering can be ignored. With an assumed average total liquid water content of 0.5 gm m^{-3} , the radiative extinction (absorption) of cloud droplets is comparable in magnitude to the extinction of raindrops at rainfall rates of about $2\text{-}5 \text{ mm hr}^{-1}$. The work of Olson (1986), Wu and Weinman (1984), and Wilhelm et al. (1982) have shown that the scattering of ice hydrometeors has a significant impact at 37 and 85.5 GHz.

As seen in Fig. 3.5c, ice has a large single scattering albedo. This is due to the fact that its volume absorption is so small. This indicates that any radiation emitted from below an ice layer will be scattered away from the radiometers field of view. With the low absorption coefficient, very

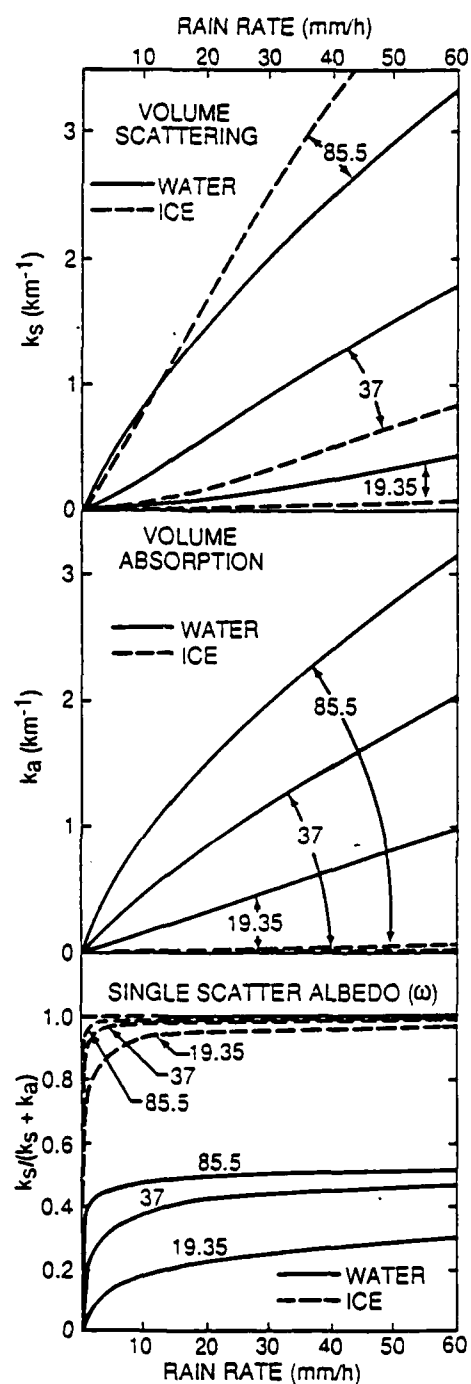


Figure 3.5. (a) Mie volume scattering coefficients. (b) Volume absorption coefficients. (c) Single scattering albedos. All are for a Marshall-Palmer precipitation size distribution of liquid and ice hydrometeors. Data is not included for the 22.235 GHz channel (Spencer et al., 1988).

little radiation will be reradiated by the ice hydrometeors. This will result in very low TB's. Notice in Fig. 3.5c that the single scattering albedo rapidly approaches unity at very low rain rates for the 85 GHz channel.

The effects of rainfall on measured TB's can be seen in Fig. 3.6. In this figure, the curve for 18 GHz will approximate the 19.35 GHz channel of the SSM/I. This study will only be concerned with rainfall over the oceans (dotted lines). For each of the three frequencies, the TB's increase rapidly up to a critical rainfall rate. This is where absorption dominates. At each frequency, as the rainfall rate increases, less of the relatively low intensity surface emission ($TB = \epsilon T$ where $\epsilon \approx 0.4$, $T \approx 300^\circ K$) is transmitted. It is replaced by higher intensity emission from the intervening cloud layer. Because the radiative extinction increases rapidly with increasing frequency as shown by Figs. 3.5a and 3.5b, so does the rate of increase in TB. So while a modest increase in TB at 18 GHz occurs over a rainfall rate of 0-20 mm hr⁻¹, a rapid change occurs at 85.5 GHz over a very small rainfall rate of 0-2 mm hr⁻¹.

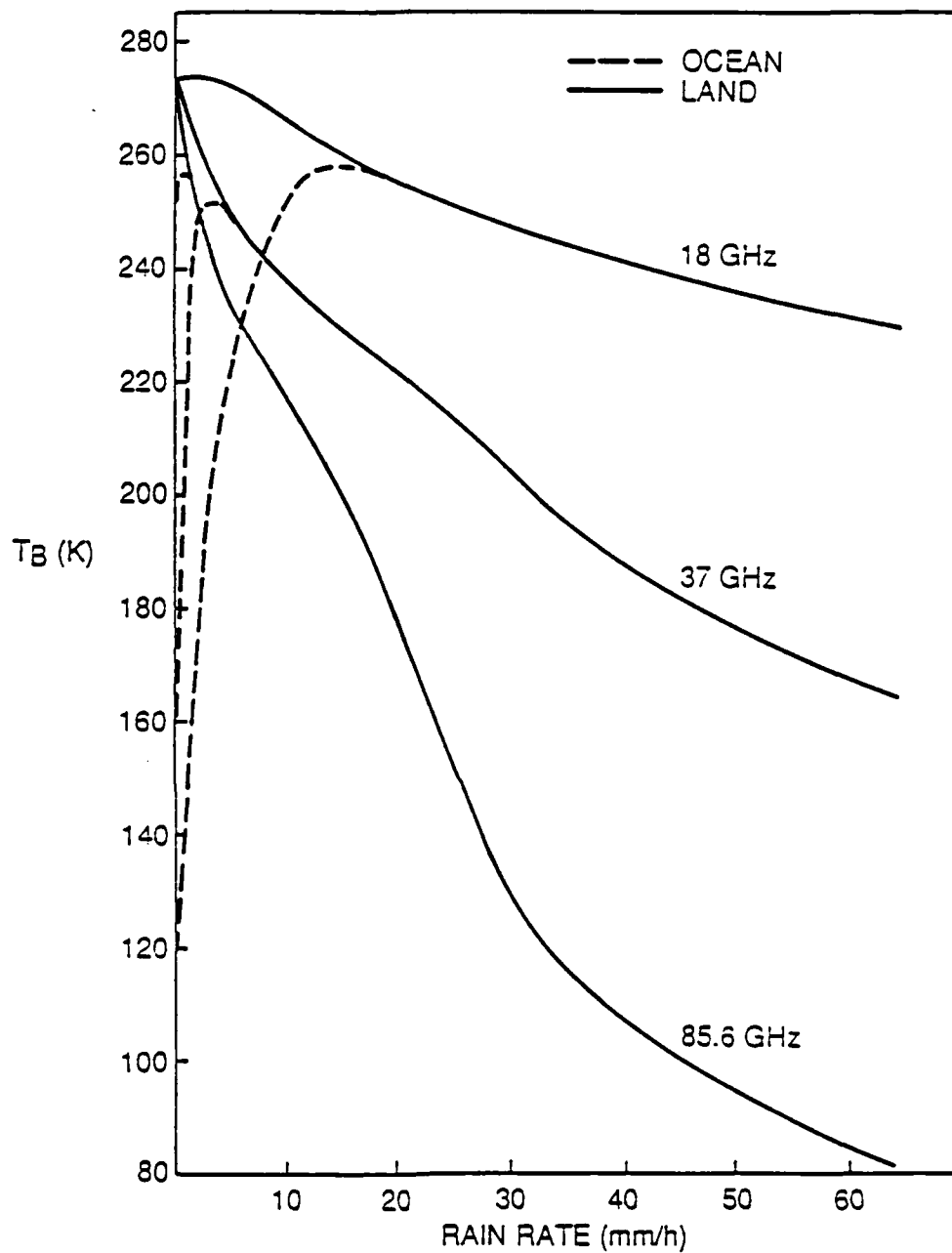


Figure 3.6. Brightness temperature - rain rate relationships at 18, 37, and 85.6 GHz. Results were calculated using the radiative transfer model of Wu and Weinman (1984). The vertical distribution of hydrometeors was based upon averaged radar results and assume ice hydrometeors above and liquid hydrometeors below the freezing level (Spencer et al., 1987).

The increase in TB occurs until a critical rain rate is reached. Beyond this rain rate, the effect of absorption of the liquid hydrometeor decreases and the effect of scattering predominates. Wilheit (1977) showed that as rain rates increased, the amount of larger droplets increases. These larger drops then scatter the surface emission much more efficiently. This causes the TB to decrease with increasing rainfall rate due to backscattering of low intensity emission from space (Olson, 1986). This decrease in TB may also be due to emission at higher and colder levels in the atmosphere. At low frequencies this scattering effect is mainly due to the larger raindrops, which scatter more efficiently. However at the higher frequencies, 37.0 and 85.5 GHz, this scattering is due to ice hydrometeors present in the cloud layer. At these frequencies, the thicker the ice layer, or the larger the concentration of ice, the greater the radiative scattering and the greater the TB decrease.

d. Changes in surface emission

As has just been shown the effects of absorption and scattering by various sized particles will have a definite impact on the TB

measured by the SSM/I radiometer. Along with this, changes in the background emissivity will affect the measured TB. This study is only concerned with tropical storms over oceanic regions, so only changes in the emissivity of the ocean and how this will change the TB measured by the SSM/I will be studied.

As mentioned earlier, because TB's are a function of the surface emissivity, what can change the emissivity has to be known. There are two ways to change the emissivity of the ocean; increases in wind speed or rainfall. The work of Wilheit (1979) and Olson (1986) show that as wind speeds increase, there is an increase in the surface roughness (waves) and foam caused by the breaking of the waves. Since this causes the reflectivity of the ocean surface to decrease, the emissivity ($\epsilon = 1 - r$) increases. This creates enhanced surface emission leading to an increase in TB as compared to calm conditions. Earlier work by Norberg et al. (1971) showed the existence of a nearly linear relationship between the increase in microwave emission of an ocean surface and an increase in wind speeds. This linear relationship is valid for wind speeds greater than 7 m s^{-1} . At wind speeds less than 7 m s^{-1} , there doesn't appear to be a

large enough increase in surface waves to cause the formation of a large amount of foam.

Fig. 3.7 shows the response of brightness temperatures at 19.35, 22.235, and 37.0 GHz to changes in the wind speeds over an ocean surface. This figure is for a clear tropical atmosphere. This figure illustrates that higher surface emission is indicated in the vertical polarization than in the horizontal at all frequencies. However, the horizontal polarization is more sensitive to the emission changes due to wind speeds than in the vertical.

Rain impaction can cause changes in the surface emissivity. But according to Olson (1986) the effect on emissivity by wind is more dominant than rain impaction.

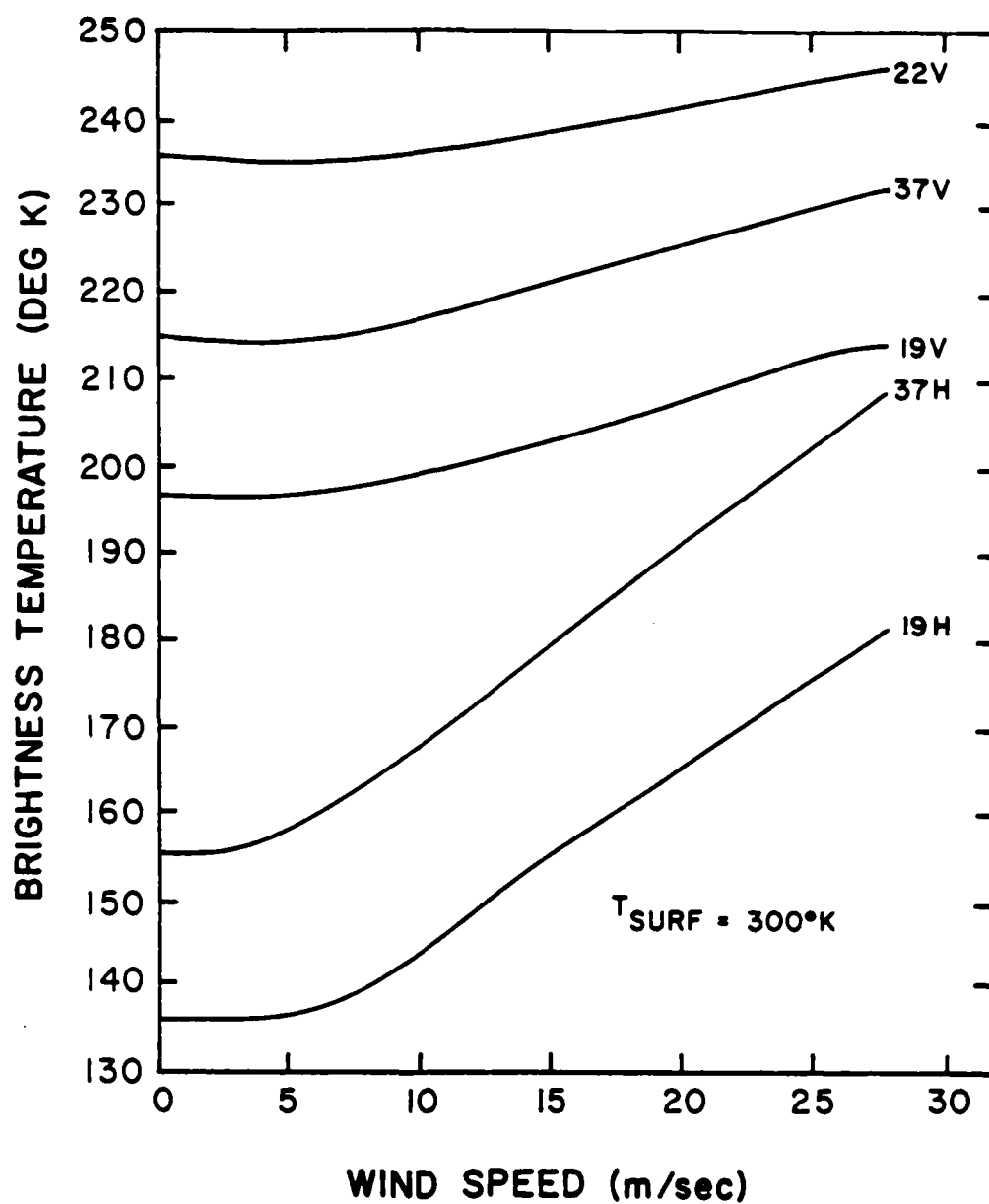


Figure 3.7. Brightness temperatures as a function of frequency, polarization (V = vertical, H = horizontal), and wind speed (Hollinger et al., 1987).

4. SSM/I DERIVED RAIN RATES

a. Latent heat release

Historically, rainfall measurements over the oceans have been poorly made, if made at all. Except for satellite measurements, there are no means to estimate rainfall over the entire ocean surface. Ship observations suffer from inaccuracy due to platform instability and sea-spray contamination. Island reports are not representative of the surrounding oceanic areas, possibly due to orographic and diurnal influences. Radar has helped, but problems with attenuation and calibration of the signal, as well as the relatively fixed nature of the radar make it unsuitable for large-scale measurements.

The best way to measure global oceanic rain rates seems to be with satellites. Several techniques have been developed which use infrared or visual satellite data to infer rain rates, however none of these provide a direct measurement. Satellite microwave radiometers enable a more accurate measurement of world-wide rain rates. The release of latent heat in precipitation areas such as tropical cyclones can then be calculated.

Many authors have pointed out the importance of the release of latent heat, through condensation processes, on the maintenance of tropical storms (e.g. Palmen and Riehl, 1957). While tropical cyclone intensification does not appear to be solely dependent on latent heat release (LHR), it is theorized that Conditional Instability of the Second Kind (CISK) is closely related. The ability to specify accurate estimates of LHR may help our modeling of tropical cyclones (Anthes, 1982).

Previous work of estimating LHR in tropical cyclones was done using the moisture budget approach with conventional and aircraft wind and water vapor measurements. But it is not particularly feasible to continuously monitor LHR in a tropical cyclone over the open ocean with this technique. As stated by Rodgers and Adler (1981), a better approach to frequent monitoring of tropical cyclone LHR is through the use of passive microwave radiometers flown on satellites, such as the SSM/I.

In this chapter a method similar to the one used by Rodgers and Adler (1981) using Nimbus-5 ESMR data will be evaluated using the SSM/I derived rain rates. A total of 23 satellite passes covering 12 tropical cyclones were used to

calculate LHR. The cyclones were in various stages of development or decay. In order to be considered for this study the center of the cyclone, at the time the SSM/I passed over it, had to be within three degrees latitude of the satellite subtrack. This would ensure sufficient data to do a complete LHR calculation.

b. Data analysis

The rain rates obtained from the SSM/I EDR's were plotted on a 1:5,000,000 scale mercator-projection base map. For each storm, a grid covering the entire storm circulation was made. The rain rate for each SSM/I pixel was manually interpolated to the nearest quarter of a degree and plotted onto the grid. If two pixels were interpolated to the same grid point, the higher rain rate of the two was plotted.

Once the rain rates for each maptime had been plotted, an average rain rate was computed for areas of 111, 222, and 444 km radius from the center of the cyclone. The average rain rate was computed by using all data pixels inside each radii, even if no rain was indicated. The center of the cyclone was determined from the Annual

Tropical Cyclone Report (Joint Typhoon Warning Center (JTWC), 1987).

The LHR was computed using the following formula:

$$LHR = L\rho \int_A R da \quad (7)$$

where L is the latent heat of condensation ($2.5 \times 10^6 \text{ J kg}^{-1}$), ρ is the density of water ($1.0 \times 10^{-3} \text{ kg m}^{-3}$), da is the incremental area, and A is the area of integration. The integration was calculated over a circular area with a radius of 111, 222, and 444 km. As in Rodgers and Adler (1981), the precipitation intensity parameter (PIP) was also calculated. The PIP is defined as the fraction of rain contributed by rain rates greater than 5 mm hr^{-1} .

The LHR and PIP results for all storms were combined to find possible relationships between these and the tropical cyclones intensity, as measured by the maximum surface wind speeds. The satellite fix data supplied by JTWC was used as the "truth". Specifically, satellite fix data is used to determine the storms maximum wind speeds and minimum sea level pressure. This is accomplished with the use of the Dvorak technique. While the Dvorak technique is very subjective, it

is generally recognized as being valid and accurate.

c. Results of LHR calculations

The rainrates, LHR, and PIP calculations for the individual cyclones are shown in Table 4.1. The average rain rates at 111, 222, and 444 km radius for the 18 mature cyclones (winds $\geq 32.5 \text{ m s}^{-1}$) are compared in Table 4.2 to those done by Rodgers and Adler (1981), and various authors using the moisture budget technique. The average SSM/I rain rates for this study were comparable to Rodgers and Adler (1981) at all radii. Our values are consistently low because Typhoons Alex (25 Jul 1987), and Betty (13 Aug 1987) plus Hurricane Florence (10 Sept 1988) had SSM/I pixels which contained coastal topography. The SSM/I coastal zone is one pixel wide at 19.35 GHz. In these regions no EDR's are computed. So for these three storms, a percentage (10-15 %) of the pixels inside the 444 km radius were treated as indeterminate by the SSM/I, and no rain rates were computed. It is probable that some of these pixels contained rain. This would have slightly increased the average rain rate for all radii, but probably not more than a few percent.

Table 4.1 Results of LHR ($\times 10^{14}$ W), average rain rate (mm hr^{-1}), and PIP calculations.

STORM	DATE/ TIME(UTC)	WIND SPEED (m s^{-1})	LHR	AVERAGE RAIN RATE			PIP
				R_{111}	R_{222}	R_{444}	
FLORENCE	9 SEPT 88 1145	27.5	2.78	2.39	1.48	0.65	0.65
	10 SEPT 88 0015	35.0	3.84	0.88	0.67	0.89	0.88
LYNN	17 OCT 87 2005	32.5	11.88	3.57	4.43	2.76	0.14
	18 OCT 87 0840	38.5	9.26	3.42	4.70	2.15	0.10
	24 OCT 87 2201	32.5	5.34	3.32	2.64	1.24	0.39
	25 OCT 87 1035	27.5	3.91	2.30	2.01	0.91	0.37
	25 OCT 87 2150	22.5	1.16	1.34	1.01	0.27	0.13
	26 OCT 87 1023	17.5	0.90	0.82	0.58	0.21	0.07
ALEX	25 JUL 87 2200	32.5	6.97	3.73	2.60	1.62	0.24
	27 JUL 87 1020	32.5	1.37	3.43	1.30	0.32	0.53
WYNNE	25 JUL 87 2020	45.0	4.39	5.16	2.96	1.02	0.21
BETTY	13 AUG 87 1020	45.0	7.03	5.14	3.94	1.64	0.33
DINAH	24 AUG 87 2100	45.0	8.30	5.23	5.10	1.93	0.27
	25 AUG 87 0935	57.5	12.56	5.27	3.90	2.92	0.33
HOLLY	9 SEPT 87 0810	63.5	8.07	3.21	3.45	1.87	0.08
NINA	22 NOV 87 2110	45.0	9.81	4.89	3.59	2.28	0.32

Table 4.1 (continued)

STORM	DATE/ TIME(UTC)	WIND SPEED (m s ⁻¹)	LHR	AVERAGE RAIN RATE			PIP
				R ₁₁₁	R ₂₂₂	R ₄₄₄	
CARY	14 AUG 87 2120	38.5	8.95	5.00	3.03	2.08	0.18
FREDA	6 SEPT 87 0845	27.5	8.39	3.98	1.90	1.95	0.28
	11 SEPT 87 0930	45.0	9.30	1.18	3.19	2.16	0.29
IAN	28 SEPT 87 0920	32.5	3.23	3.03	2.57	0.75	0.20
KELLY	12 OCT 87 2105	38.5	8.76	3.47	4.80	2.04	0.24
	13 OCT 87 2050	38.5	7.78	2.57	3.36	1.81	0.11
	14 OCT 87 0930	38.5	4.52	2.82	2.26	1.05	0.19
<hr/>							
			AVERAGES				
ALL CYCLONES			6.50	3.31	2.85	1.50	0.28
18 MATURE CYCLONES			7.30	3.63	3.26	1.68	0.28

TABLE 4.2 Mean rain rate comparisons for mature cyclones (mm hr⁻¹).

	Radius of area covered (km)		
	111	222	444
Present study	3.6	3.3	1.7
Rodgers and Adler (1981)	4.2	3.4	1.9
Frank (1977)	-	3.9	2.2
Marks (1985)	2.7	-	-

The average LHR within 444 km of the center of the cyclone for all 23 cases was 6.5×10^{14} W. For the 18 mature cases the average LHR was 7.3×10^{14} W. Once again this is in reasonable agreement with Rodgers and Adler (1981) results of 8.7×10^{14} W. The average PIP for all 23 cases was 0.28.

Fig. 4.1 shows how the LHR and maximum surface winds were related for the 23 cases. The linear correlation was 0.62. The t-distribution test determined this to be significant at the 1% level. This is also very close to the 0.71 correlation computed by Rodgers and Adler (1981). As seen, Typhoon Holly seems to be an anomaly compared to the rest of the data. Chapter 6b will discuss why Holly seems to be so different. If Holly is removed from Fig. 4.1 the correlation coefficient increases to 0.68.

Rodgers and Adler (1980) correlated the PIP values with cyclone intensity. They found a correlation of 0.52 which was less than the corresponding correlation between LHR and cyclone intensity. When the PIP data calculated from the 18 mature cyclones (wind speeds $\geq 32.5 \text{ m s}^{-1}$) were correlated with cyclone intensity in this study a negative correlation of -0.20 was found. The exact

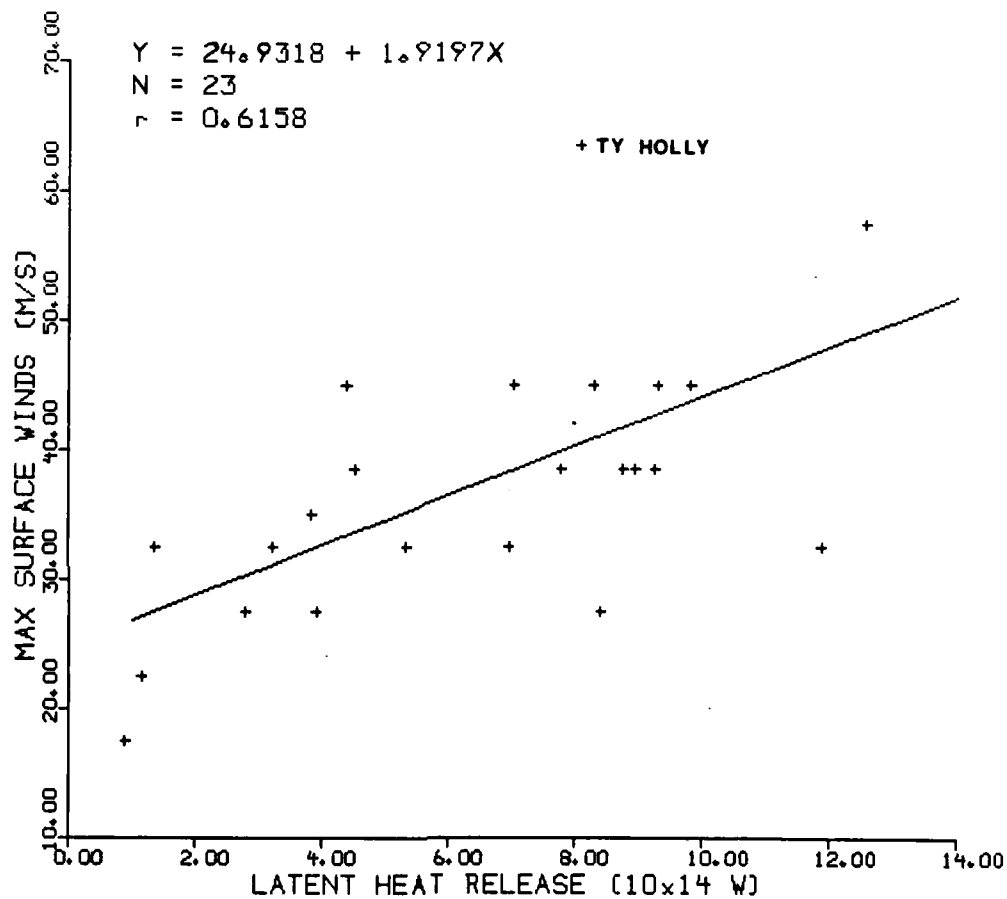


Figure 4.1. Scatter plot of cyclone intensity versus latent heat release for 23 cases. Equation of best fit line, number of cases, and correlation coefficient are shown in the upper left hand corner.

reason, for this is not known, however it appears that many of the cyclones used in this study were characterized by large areas of uniform rain with rain rates of 5 mm hr^{-1} or less resulting in low PIP values.

Another factor which may have created this negative correlation is that of the 18 mature cyclones, six weakened in intensity in the 36 hours following the SSM/I pass which was used in the rain rate study. Rodgers and Adler (1981) found that the maximum intensity was reached 1-2 days after the maximum LHR was obtained. Because one third of the cyclones used in this study weakened in the 36 hours after the SSM/I pass, it seems reasonable to expect that their maximum LHR had already been reached and their rain rates and PIP values were declining at the time of the SSM/I pass. This would then have a negative effect on the rest of the data when a correlation was computed.

d. Observations of rainband structure

One advantage of using microwave radiometric data is the ability to penetrate thick cloud layers and detect the structure of convective rainbands. This is not possible with visible and

infrared satellite data because the thick cirrus at the top of the cloud layers will absorb at infrared wavelengths and scatter at visible wavelengths.

Even though the SSM/I has the ability to observe the rainband structure, because of its large field of view (approximately 800 km^2) the measured rain rates will tend to be an average over this area. As a result rain rates in the heavier convective regions near the eyewall are grossly underestimated.

Figs. 4.2 through 4.4 show the SSM/I derived rain rate pattern for Typhoons Dinah, Holly, and Wynne. In all three figures the SSM/I shows the rainband structure as well as the asymmetry of the rainbands. Fig. 4.2 shows a maximum rain rate of 12 mm hr^{-1} just south of the eye of Typhoon Dinah. The asymmetry of Dinah is very apparent. While a strong band of convection, with rain rates greater than 6 mm hr^{-1} , exists from southwest through northeast of the cyclone, only a small area of rain rates greater than 4 mm hr^{-1} appears on the west or north side of the cyclone. Evidence of a large feeder band can be seen as an appendage in the rain rates on the east side.

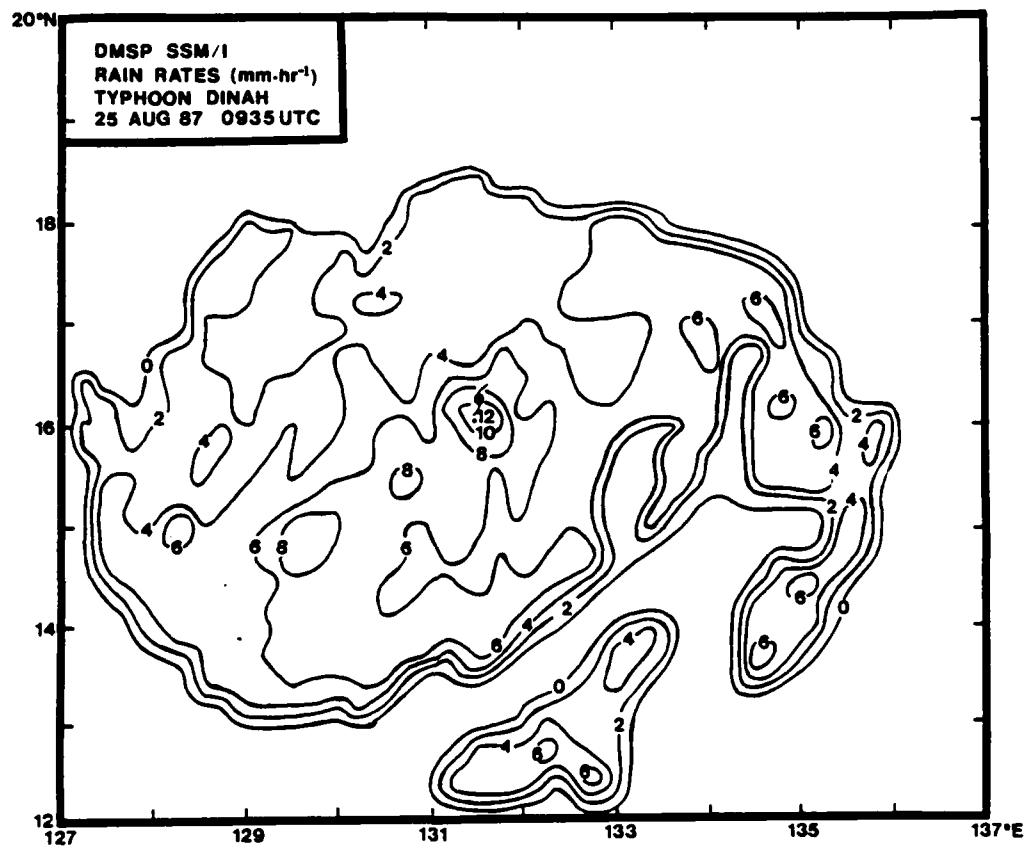


Figure 4.2. Plot of SSM/I rain rates for Typhoon Dinah

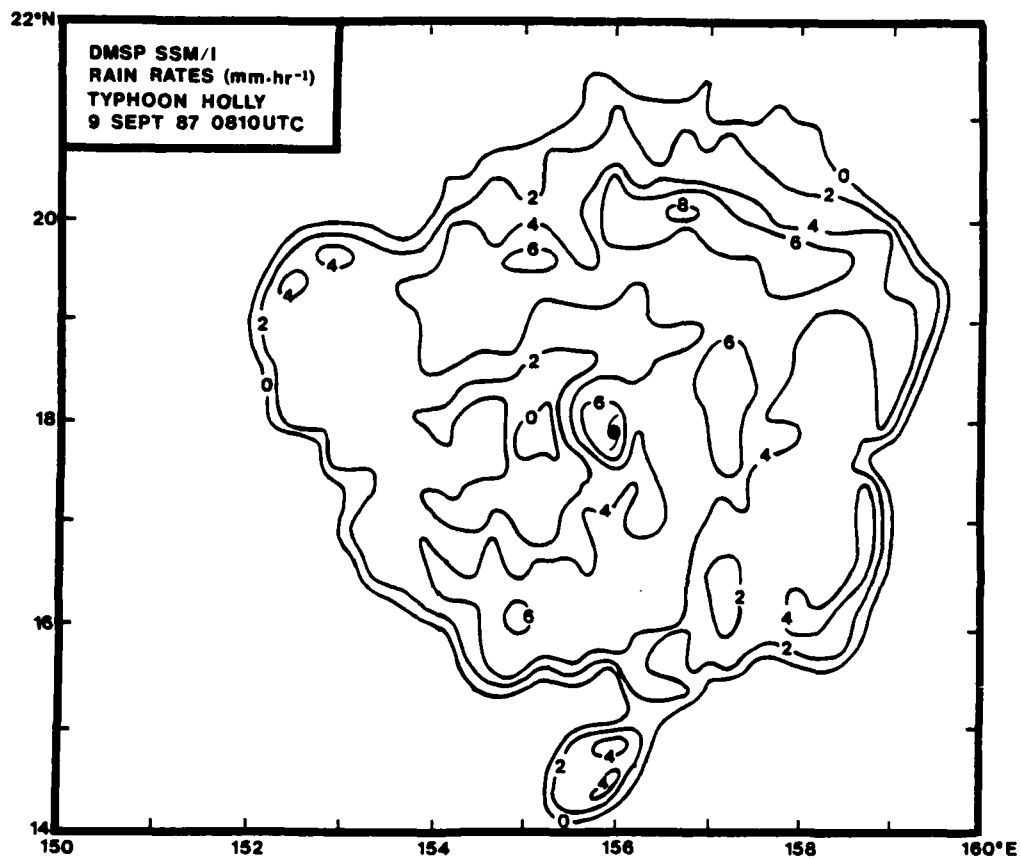


Figure 4.3. As in Fig. 4.2 except for Typhoon Holly.

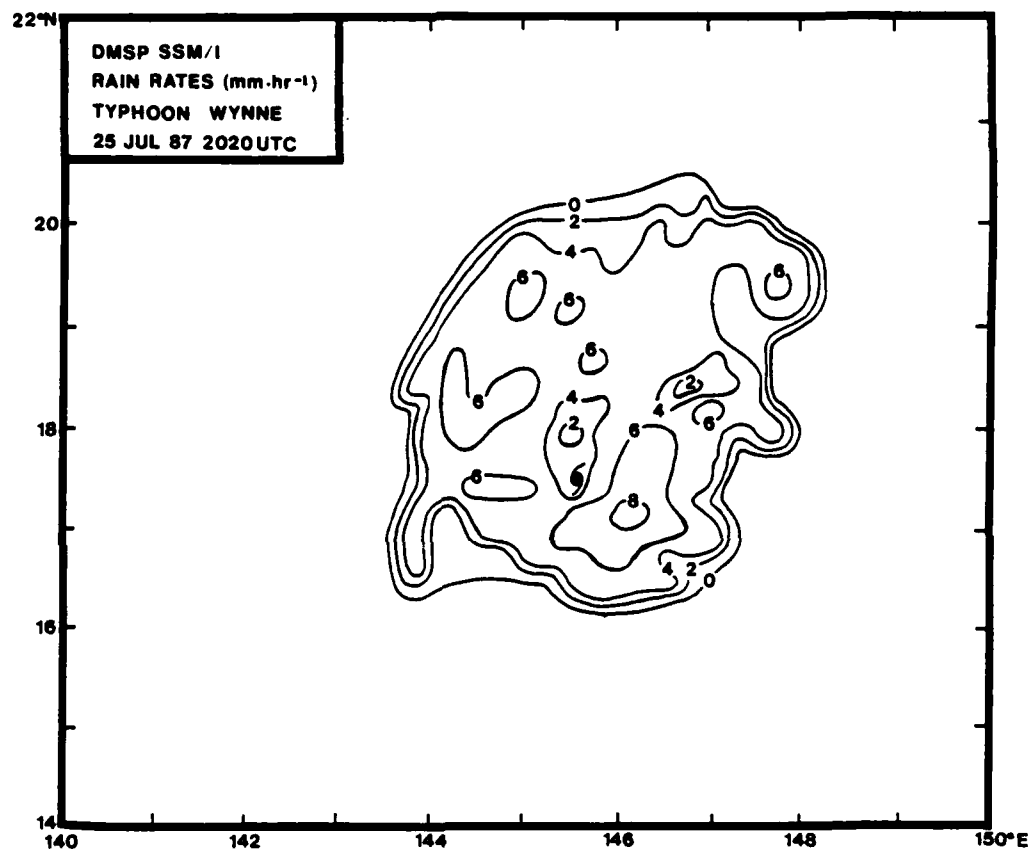


Figure 4.4. As in Fig. 4.2 except for Typhoon Wynne.

Fig. 4.3 shows the core region of Typhoon Holly as an area with rain rates greater than 6 mm hr^{-1} surrounding the center. The asymmetry of the rainbands is once again very evident with rain rates greater than 6 mm hr^{-1} from the northwest through the northeast, east, and south of the cyclone center. A relatively dry area shows up west of the center.

Typhoon Wynne is shown in Fig. 4.4. This cyclone was described by the forecasters at JTWC as a "midget" typhoon. This can be seen by its small area of rain. Typhoon Wynne had a strong band of convection (rain rates greater than 6 mm hr^{-1}) to the southeast of the center.

5. SSM/I DERIVED WIND SPEEDS

a. Data analysis

As discussed in chapter 3d, changes in the surface emissivity of the ocean will cause changes in the observed brightness temperature. One way to change the emissivity of the ocean is to increase the wind speed over its surface. The SSM/I has the ability to sense these changes in emissivity and determine the resulting wind speed. In this section a large data base is developed which will determine the accuracy of the SSM/I derived wind speeds.

The TB's measured by the SSM/I are used in a set of linear regression equations to determine various environmental parameters (EDR's). Wind speeds over the oceans are one of these parameters. To calculate wind speeds at any particular pixel point, the following regression equation is used:

$$W = C_0 + C_1 \cdot TB(19H) + C_2 \cdot TB(22) + C_3 \cdot TB(37V) + C_4 \cdot TB(37H) \quad (8)$$

where C_0, C_1, C_2, C_3 , and C_4 are coefficients which depend on the latitude of the pixel, as well as the time of year. These coefficients have been

determined based on radiative transfer modeling, geophysical models, an inversion algorithm, and climatology. Hollinger et al. (1987) discuss this dependence in greater detail and also list the original values of the coefficients. In September 1988 these coefficients were given new values based on the recommendation of researchers using the original coefficients. With the original coefficients, the SSM/I derived wind speeds showed a large positive bias ($3-6 \text{ m s}^{-1}$) at low wind speeds ($0-12 \text{ m s}^{-1}$), as well as a smaller negative bias at high wind speeds ($30+ \text{ m s}^{-1}$). This study used the new set of coefficients.

The derived wind speeds using the revised coefficients were compared to land and ship observations. It is known that surface winds as measured by land based stations are generally not representative of winds over the open ocean due to surface friction and differences in the thermal structure. Therefore a correction to the land based wind speed measurements must be made. Hsu (1986) studied many pairs of onshore and offshore wind measurements under various wind conditions. The following linear regression equation was derived by Hsu:

$$U_{\text{sea}} = 1.62 + 1.17 \times U_{\text{land}} \quad (9)$$

where the wind speeds are in meters per second. Although (9) does not take into account the air-sea temperature differences, Hsu found the results to be satisfactory.

In order to be used in this study, a SSM/I data pixel had to meet certain spatial and temporal criteria. Initially it had to be within 30 nm and ± 3 hours of the verifying land/ship data point. Furthermore, the verifying land and ship reports should report no precipitation. This is to eliminate any contamination by rainfall interfering with the emissivity of the ocean surface (see chapter 3d). The value of 30 nm was chosen because the SSM/I algorithm will not compute EDR's within one pixel of the coast. Because there is a 25 km distance between successive pixels for the channels used in the wind speed algorithm, 30 nm was a large enough distance to ensure this was not a problem. The closest SSM/I pixel to the verifying land/ship observation was used.

Several different methods were used to evaluate the SSM/I derived wind speeds. Once all the data pairs were collected, a statistically based evaluation was made. Two types of best fit curves were then applied to the data: linear and

semi-logarithmic. For all these methods, data for six cyclones with the following SSM/I passes were used :

Thelma

13 Jul 87 @ 2100 UTC

14 Jul 87 @ 0941 UTC

Vernon

20 Jul 87 @ 1010 UTC

21 Jul 87 @ 1000 UTC

Alex

26 Jul 87 @ 1030 UTC

27 Jul 87 @ 1025 UTC

Floyd

12 Oct 87 @ 2330 UTC

13 Oct 87 @ 1040 UTC

Lynn

24 Oct 87 @ 2200 UTC

25 Oct 87 @ 1030 UTC

25 Oct 87 @ 2150 UTC

26 Oct 87 @ 1020 UTC

Susan

1 Jun 88 @ 2215 UTC

b. Results

The results of this wind verification study are shown in Table 5.1. In the first case study, the SSM/I pixels met the 30 nm and ± 3 hour criteria (see earlier discussion). A total of 799 data pairs were evaluated. The results are shown in column A of Table 5.1. The values for A, B, a, and b denote constants used in the linear and nonlinear equations, while r is the correlation coefficient. The scatter diagram for the linear fit in column A is shown in Fig. 5.1. Compared to the old coefficients, the new set does a much better job at the low wind speeds. However, both the linear and semi-log equations badly underestimated the winds when the speeds were greater than 16 m s^{-1} .

One of the inherent problems in using the SSM/I data is the size of the footprint. Of the four frequencies used in the wind speed algorithm, the 37 GHz channel has the smallest footprint at approximately 800 km^2 . Because of this, the wind speed derived by the SSM/I will be an areal averaged value over this footprint. There is a problem comparing this value to an in situ measurement. While it's not possible to change the

TABLE 5.1 Results of wind speed study

WIND SPEED (m/s)	COL A		COL B		COL C		COL D	
	LIN	NLIN	LIN	NLIN	LIN	NLIN	LIN	NLIN
4	6.98	6.63	7.93	6.90	13.74	13.20	14.73	14.04
6	7.99	7.33	8.71	7.71	14.77	13.86	15.68	14.68
8	8.99	8.11	9.48	8.61	15.79	14.56	16.63	15.35
10	10.00	8.96	10.26	9.62	16.82	15.19	17.59	16.05
12	11.01	9.91	11.04	10.75	17.85	16.06	18.54	16.78
14	12.01	10.96	11.81	12.00	18.88	16.86	19.50	17.55
16	13.02	12.12	12.59	13.41	19.91	17.71	20.45	18.35
18	14.03	13.40	13.37	14.98	20.94	18.60	21.41	19.18
20	15.03	14.81	14.15	16.74	21.97	19.53	22.36	20.06
22	16.04	16.37	14.92	18.70	22.99	20.51	23.32	20.97
24	17.04	18.10	15.70	20.89	24.02	21.54	24.27	21.93
26	18.05	20.02	16.48	23.34	25.05	22.63	25.23	22.93
28	19.05	22.13	17.25	26.07	26.08	23.76	26.18	23.98
30	20.07	24.47	18.03	29.13	27.11	24.96	27.14	25.07
32	21.07	27.05	18.81	32.54	28.13	26.21	28.09	26.21

The formats for the curves are:

Linear: $Y=A + Bx$

Nonlinear: $Y=aexp(bx)$

Column

A: SSM/I winds within ±3 hours and ±30 Nm. (n=799)

A= 4.9675 B= 0.5032 r= 0.6248

a= 5.4265 b= 0.0502 r= 0.5721

B: SSM/I winds within ±1 hour and ±30 Nm. (n=258)

A= 6.3740 B= 0.3886 r= 0.4063

a= 5.5270 b= 0.0554 r= 0.4202

C: Same criteria as column A, however rain was indicated by the verifying observation. (n=210)

A= 11.6796 B= 0.5143 r= 0.3207

a= 11.9661 b= 0.0245 r= 0.2765

D: Same as column C, but the time criteria is ±1 hour. (n=156)

A= 12.8155 B= 0.4774 r= 0.2886

a= 12.8412 b= 0.0223 r= 0.2418

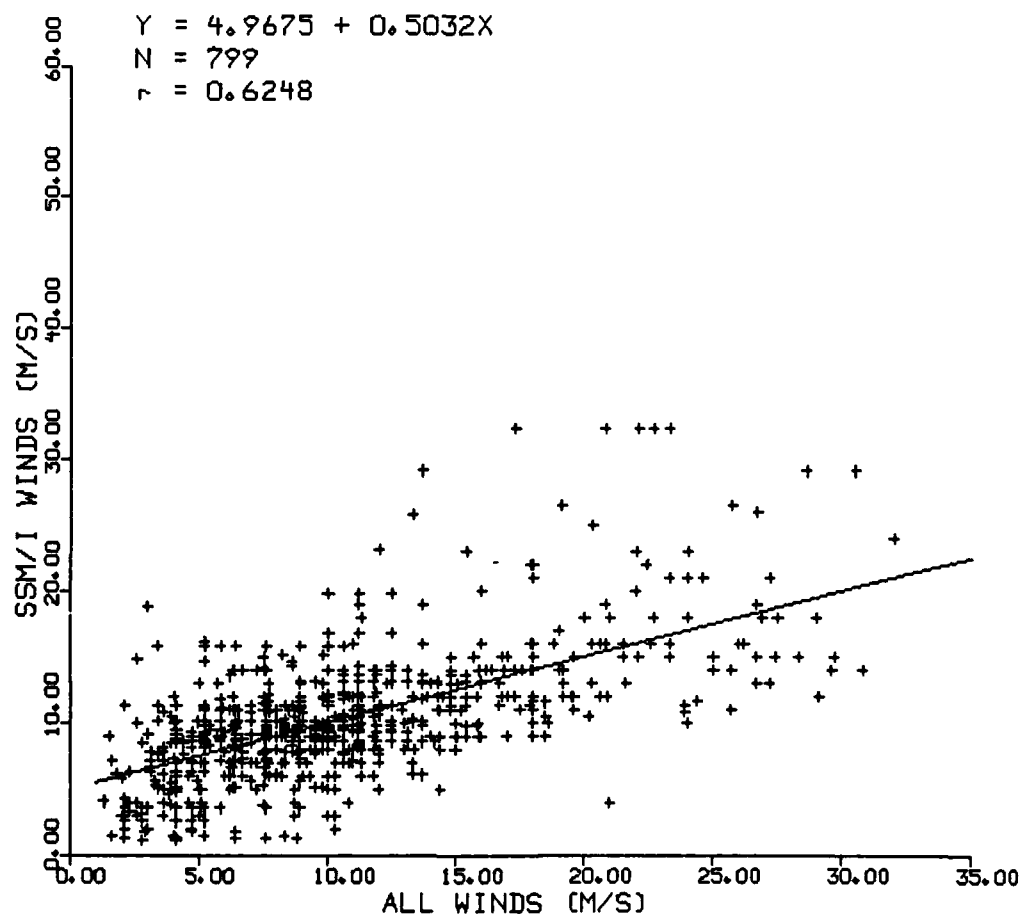


Figure 5.1. Scatter plot of SSM/I derived wind speeds versus "truth" data along with linear regression line.

size of the SSM/I footprint, it is possible to change the temporal criteria to get the SSM/I data as close in time as possible to the in situ measurement.

In the second case the temporal criteria is changed to 1 hour. The corresponding results for a total of 258 data pairs are shown in Table 5.1, column B. While the linear fit gave results which were similar to those found in column A, the semi-log fit (Fig. 5.2) showed a marked improvement. This is especially true at wind speeds greater than 12 m s^{-1} . Because most of the data in this case was for winds less than 20 m s^{-1} , results above this value should be used with caution.

Another problem mentioned in chapter 3d is the determination of wind speeds in the presence of rain. Rain is a problem for two reasons. First, rain impaction on the surface of the ocean will tend to decrease the reflectivity of the ocean surface therefore increasing the emissivity. This could possibly lead to an overestimation of the wind speed. Secondly, the frequencies used in the wind speed algorithm (19, 22, and 37 GHz) are heavily attenuated by rain. This will mask the wind speed measurements which can be detected due to formation of foam and waves on the ocean

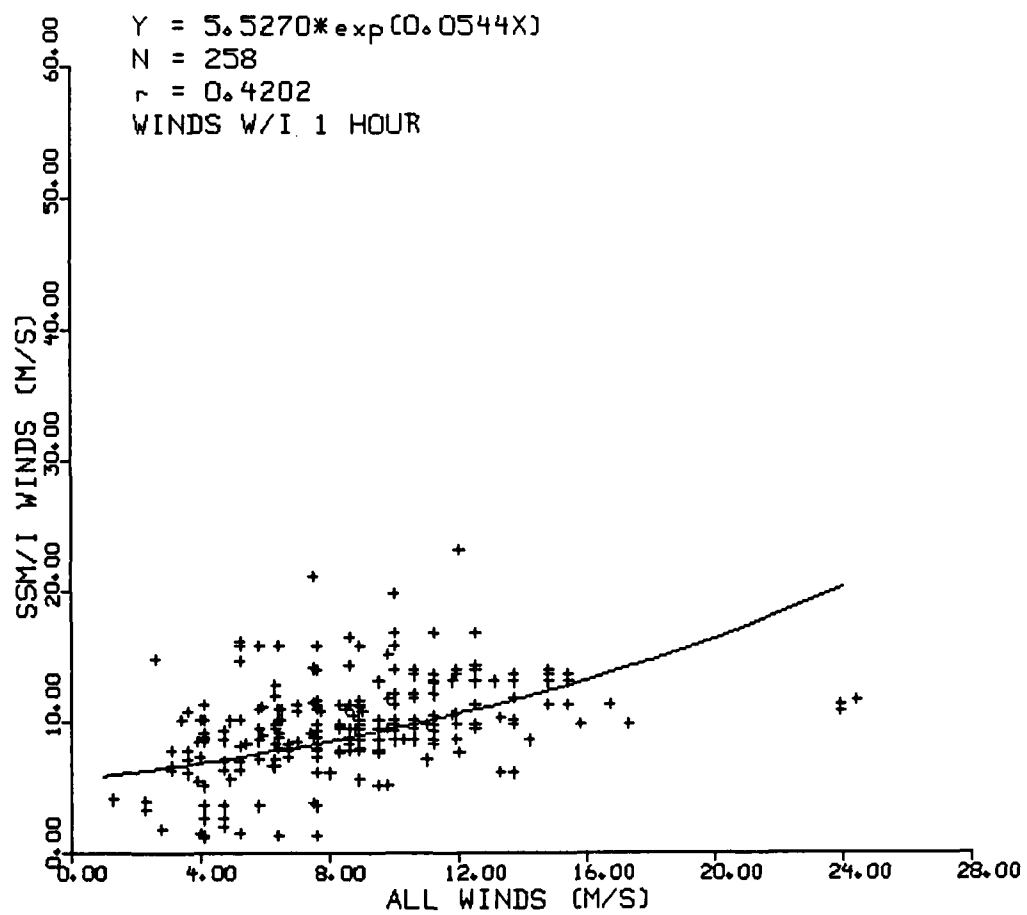


Figure 5.2. As in Fig. 5.1 except the temporal criteria is ± 1 hour and a nonlinear regression line is used.

surface. Because of this, an accurate measurement of the wind speed in the presence of rain is not possible. In columns C and D, the spatial and temporal criteria are the same as used in columns A and B respectively, but this time only data pairs where the land/ship observation was indicating the presence of rain are used. The results (Figs. 5.3 and 5.4) indicate the SSM/I overestimates at low wind speeds ($0-10 \text{ m s}^{-1}$), but improves as wind speeds increase. This seems to agree with Olson (1987) who felt that in tropical cyclones, the wind effect would dominate the rain impactation. This would especially be true at the higher wind speeds.

According to the t-distribution test, all of the results shown in this chapter were significant at less than the 1% level.

Recently, Hollinger (1989) completed an extensive review of all SSM/I derived environmental parameters. They concluded that the SSM/I derived wind speeds are most accurate near a mean of 7 m s^{-1} and become worse at wind speeds above this value. They showed a negative bias of 2 m s^{-1} for wind speeds in the range of $12-19 \text{ m s}^{-1}$. This is very similar to the results in Table 5.1, for the semi-log fit shown in column B.

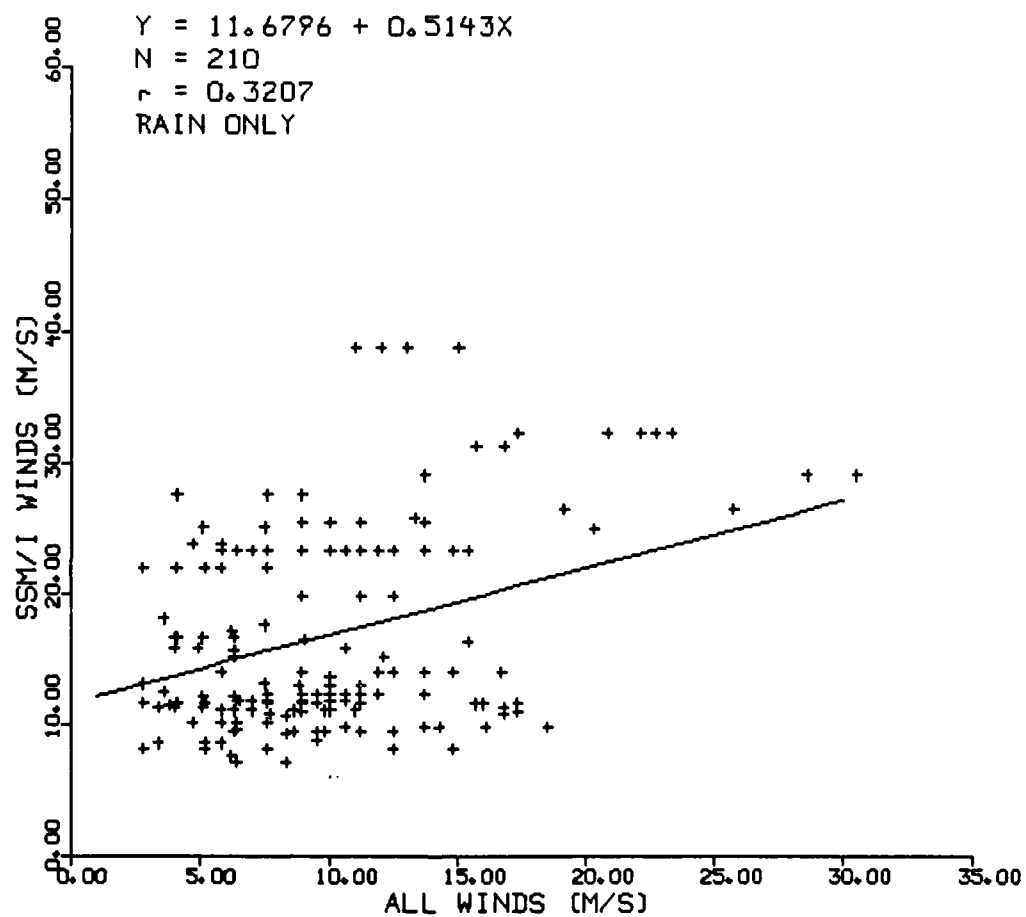


Figure 5.3. As in Fig. 5.1 except "truth" data is only for stations reporting precipitation.

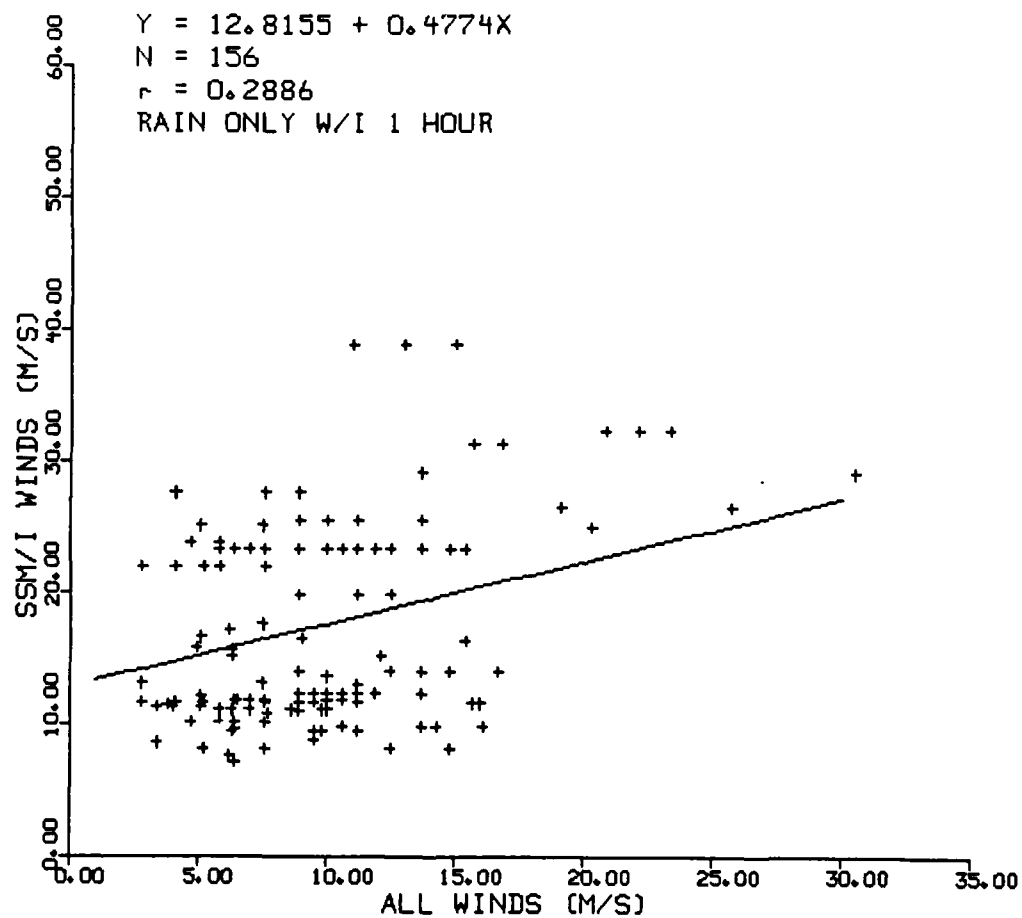


Figure 5.4. As in Fig. 5.3 except the temporal criteria is 1 hour.

Hollinger (1989) also concluded that the accuracy of the derived wind speeds deteriorates rapidly in the presence of rain. A set of four rain flags has been developed which are to be used only where rain is present, and will give accuracy limits that must be referred to under these rain conditions. Because the accuracy diminishes as rain rates increase, the ability of the SSM/I to determine wind speeds near the center of the cyclone in the presence of heavy rain is questionable.

6. 85 GHz BRIGHTNESS TEMPERATURES

a. Background and channel determination

While the SSM/I provides rain rates and wind speeds (EDR's) associated with a tropical cyclone, the SDR's (TB's) may hold a key to equally important parameters such as cyclone intensity and possibly its future development or decay. In this chapter the 85 GHz vertically polarized TB's will be used to draw some conclusions concerning cyclone intensity. Specifically, the difference in TB's between the core and the environment surrounding the cyclone will be used to find a relationship with the cyclone intensity.

Gentry et al. (1980) found a strong correlation between the measured equivalent blackbody temperatures (TBB) of cloud tops near a cyclone center and the future intensity of that cyclone. They found that the lower the mean TBB of the cloud tops over the cyclone center, the stronger and more persistent the convection. A decrease in TBB was well correlated to an increase in the maximum winds. Fig. 6.1 depicts data for two cases where the lowest TBB's were actually reached one to three days prior to the cyclone reaching its maximum wind speeds.

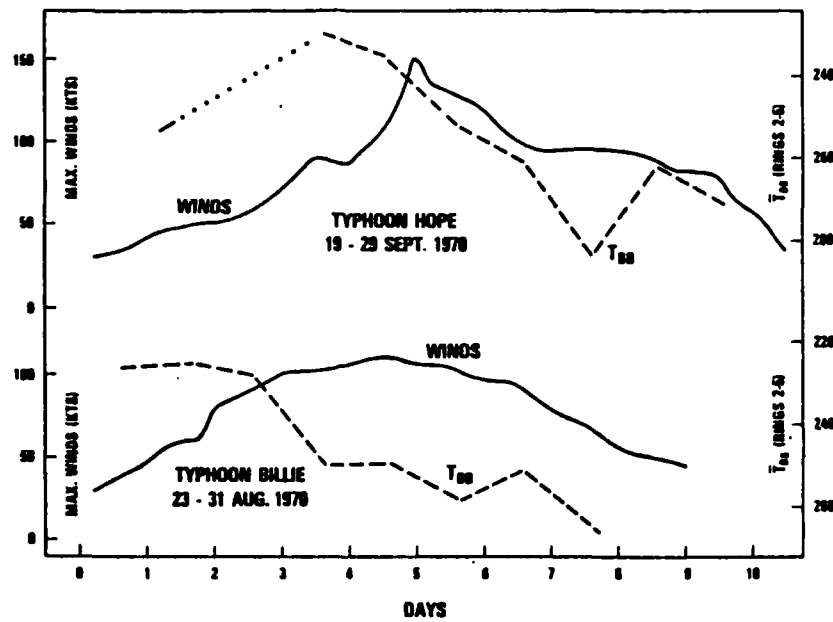


Figure 6.1. Temporal changes of mean equivalent blackbody temperatures and maximum winds of Typhoons Holly (Sept 1970) and Billy (Aug 1970). The temperature scale is inverted to show the lower temperature at the top of the graph (Gentry et al., 1980).

Kidder et al. (1978) used the 55.45 GHz data of the Scanning Microwave Spectrometer on board the Nimbus 6 satellite to estimate the central pressure and maximum winds in tropical cyclones. The weighting function of the 55.45 GHz channel peaks in the region of the maximum temperature anomaly, centered near 250 to 300 mb. Fig. 6.2 shows the correlation between the temperature anomaly and the central pressure.

A similar approach with the SSM/I data is attempted in this study. The 85 GHz channel is chosen because it shows an almost linear decrease in TB with increasing rain rates (see Fig. 3.6). This channel is very sensitive to ice hydrometeors at the top of the clouds. Because the density of ice hydrometeors and rain rate are related (Wu and Weinman, 1984), TB's will decrease with increasing rain rate and increasing thickness of the ice layer. Fig. 6.3 illustrates the variation of TB's with various rain rates at a frequency of 92 GHz. Wu and Weinman (1984) also showed the 85 GHz channel to be sensitive to the upper 3-5 km of a cloud which contains ice hydrometeors.

Figs. 6.4 and 6.5 depict west to east cross sections of Typhoons Dinah and Cary respectively. The SSM/I derived rain rates (solid) and the

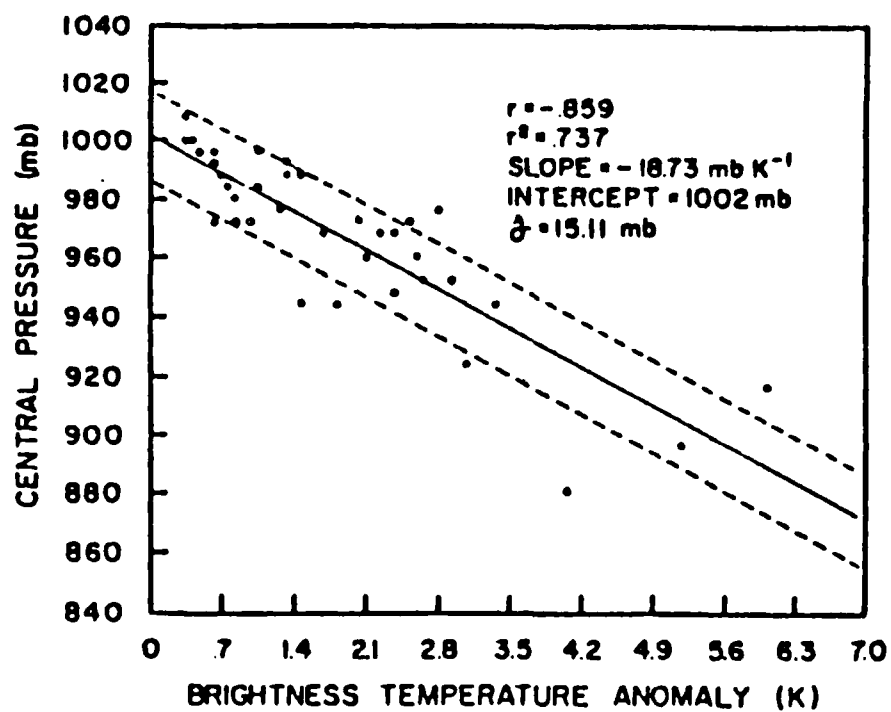


Figure 6.2. Central pressure versus maximum brightness temperature anomaly within 2° latitude of the cyclone center (Kidder et al., 1978).

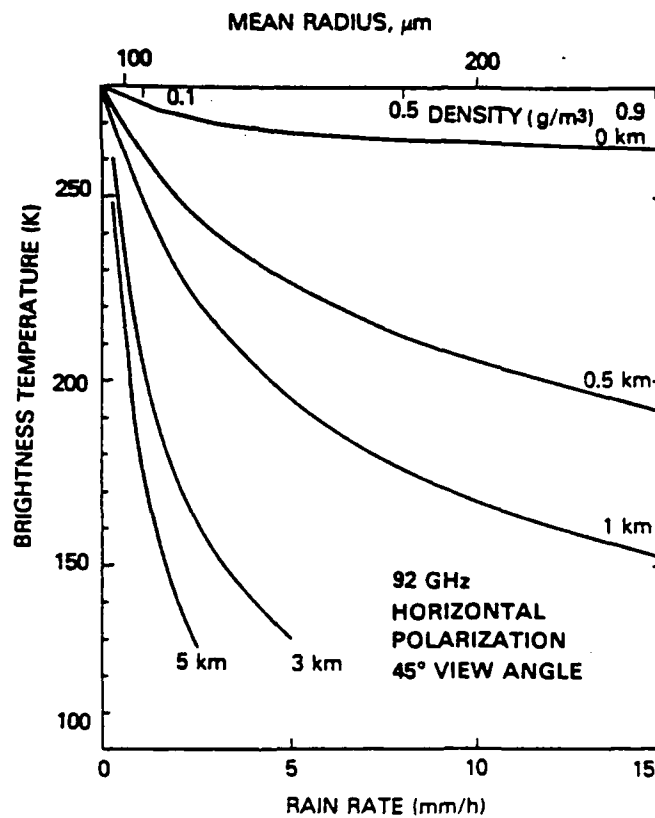


Figure 6.3. Brightness temperature calculations for 92 GHz. Values adjacent to curves indicate the thickness of the ice layer. The assumed freezing level is 5 km (Wilheit et al., 1982).

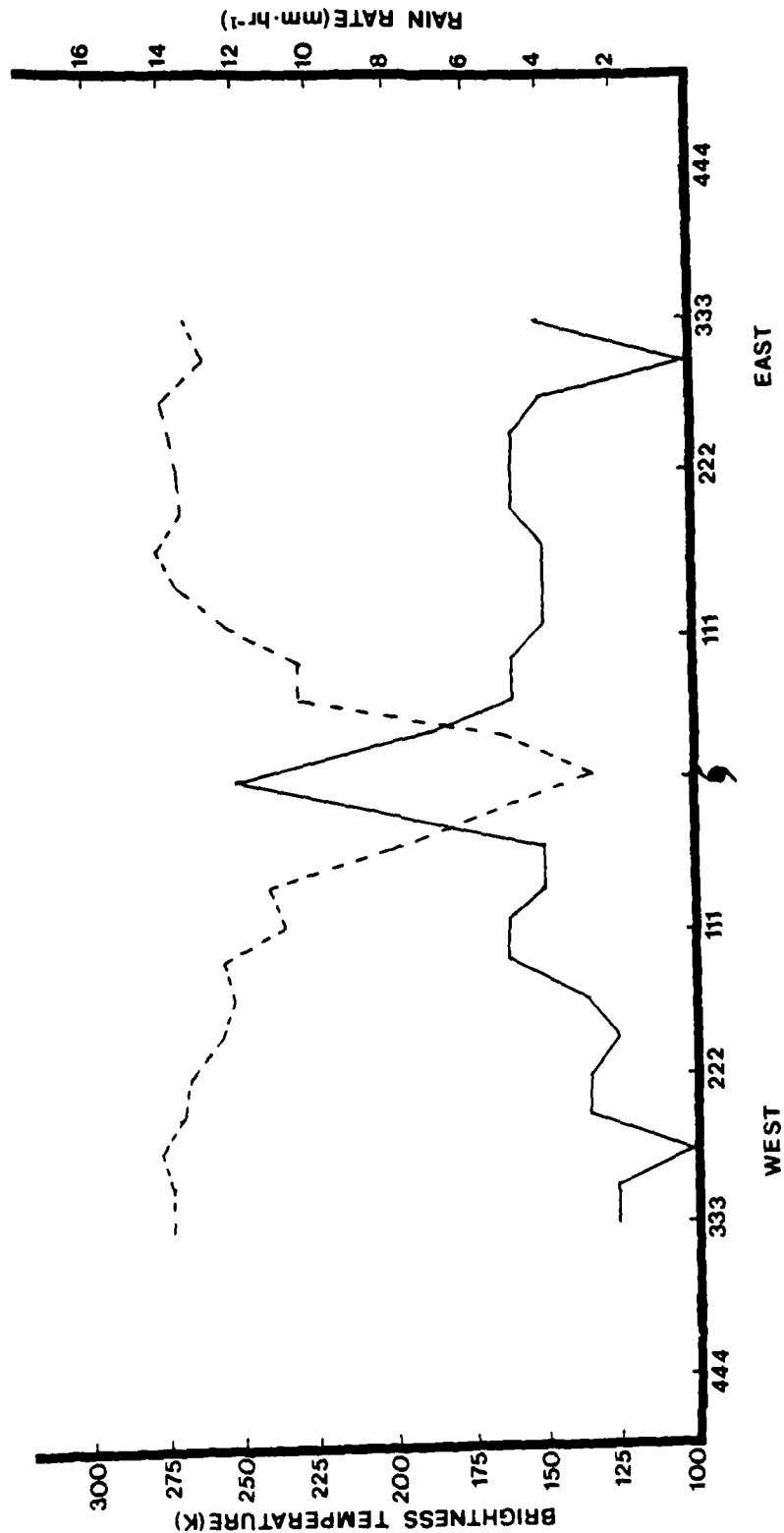


Figure 6.4. West to east cross section through Typhoon Dinah (25 Aug 1987 @ 0935 UTC). Distance in Km from the center of the cyclone are depicted on the x-axis. Dashed line represents TB's, while solid line represents rain rates.

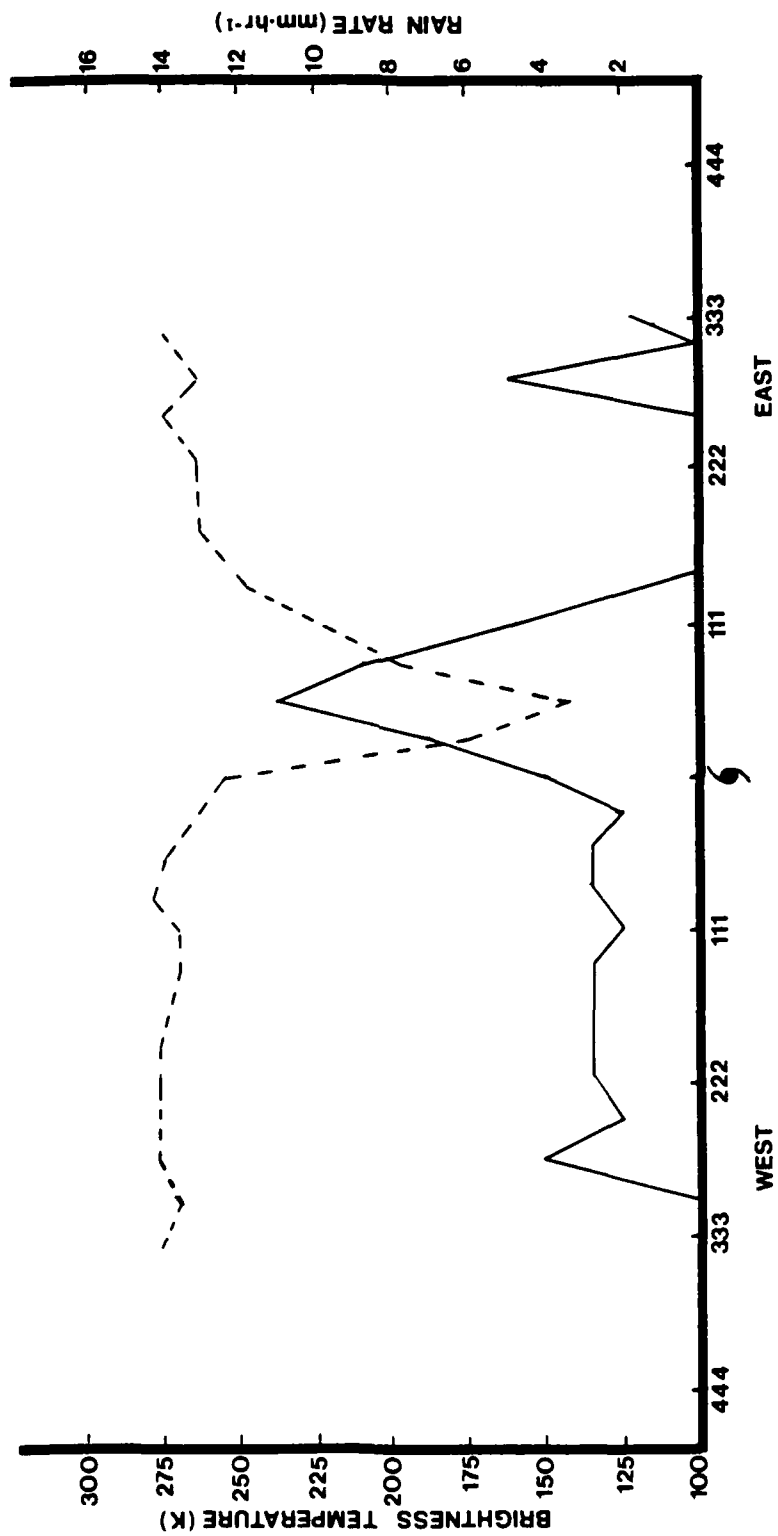


Figure 6.5. As in Fig. 6.4 except for Typhoon Cary (14 Aug 87 @ 2120 UTC).

corresponding 85 GHz vertically polarized TB's (dashed) are plotted for each quarter degree data point used in the LHR study. It is seen that as the rain rate increased, the corresponding 85 GHz TB decreased, verifying the theory proposed earlier that as the rain rate increased, the amount of ice hydrometeors also increased, leading to a decrease in the measured 85 GHz TB.

But why use the vertical polarization? Wilheit et al. (1982) determined that scattering is independent of polarization, while variations in surface properties show up more strongly in the horizontal polarization TB's. Therefore he concluded that to enhance the scattering effects, as opposed to the surface effects, the vertical polarization should be chosen.

In this study the average 85 GHz vertically polarized TB's for a $6 \times 6^\circ$ box are compared to those for inner boxes of $2 \times 2^\circ$, $3 \times 3^\circ$, and $4 \times 4^\circ$. All these boxes are centered on the cyclone (as reported by JTWC). As shown by Frank (1977) this will compare the TB's of the outer rainbands to that of the eyewall region and inner rainbands of the cyclone. Since the heaviest rain rates and largest concentration of ice hydrometeors are normally found in the eyewall and inner rainband

region of a tropical cyclone (Frank, 1977), the 85 GHz vertically polarized TB's of this region should be lower than in the surrounding rainbands. It is also postulated that the difference in average TB's between the inner and outer regions of a cyclone should increase as its intensity increases.

b. Data analysis and results

The 85 GHz vertically polarized TB's were plotted on the same type of grid used in the LHR computations in chapter 4b. The TB's were plotted every quarter of a degree, even though the 85 GHz TB is available every eighth of a degree. The size of the smaller inner box varied from $2 \times 2^\circ$, $3 \times 3^\circ$, and $4 \times 4^\circ$ for each cyclone. The temperature difference between the larger $6 \times 6^\circ$ box was compared to that of the smaller boxes. This temperature difference was then correlated to the cyclone intensity as reported by JTWC. The cyclone intensity was obtained from the Current Intensity (CI) number (Dvorak, 1984). The CI was then related to the maximum surface winds as shown in Fig. 6.6.

CI Number	MWS (Knots)	MSLP (Atlantic)	MSLP (NW Pacific)
1	25 K		
1.5	25 K		
2	30 K	1009 mb	1000 mb
2.5	35 K	1005 mb	997 mb
3	45 K	1000 mb	991 mb
3.5	55 K	994 mb	984 mb
4	65 K	987 mb	976 mb
4.5	77 K	979 mb	966 mb
5	90 K	970 mb	954 mb
5.5	102 K	960 mb	941 mb
6	115 K	948 mb	927 mb
6.5	127 K	935 mb	914 mb
7	140 K	921 mb	898 mb
7.5	155 K	906 mb	879 mb
8	170 K	890 mb	858 mb

Figure 6.6. Empirical relationship between the current intensity number (CI), the maximum mean wind speeds (MWS), and the minimum sea level pressure (MSLP) in tropical cyclones (Dvorak, 1984).

With the size of the inner box set at $3 \times 3^\circ$, Fig. 6.7 shows that generally the maximum wind speeds increased with increasing TB difference. Typhoons Dinah and Holly stood out as anomalies because high surface winds did not reveal a large TB difference. The reason for this will be explained shortly. When these two cyclones were removed, the correlation coefficient improved significantly from 0.45 to 0.70. The t-distribution test revealed this to be significant at less than the 1% level. With Typhoon Dinah and Holly included, the t-test was significant at the 2% level.

The size of the inner box was then varied to see if a better correlation could be obtained. $2 \times 2^\circ$ and $4 \times 4^\circ$ sized boxes were used. The results are shown in Figs. 6.8 and 6.9, respectively. The $2 \times 2^\circ$ area encompasses the eyewall region while the $4 \times 4^\circ$ area combines the eyewall and the inner rainbands. Once again, Typhoon Holly stood out as an anomalous storm. When this data point was removed from both data sets, the correlation coefficients for the $2 \times 2^\circ$ and $4 \times 4^\circ$ boxes increased to 0.72 and 0.78, respectively. The t-distribution test determined both cases to be significant at the 1% level.

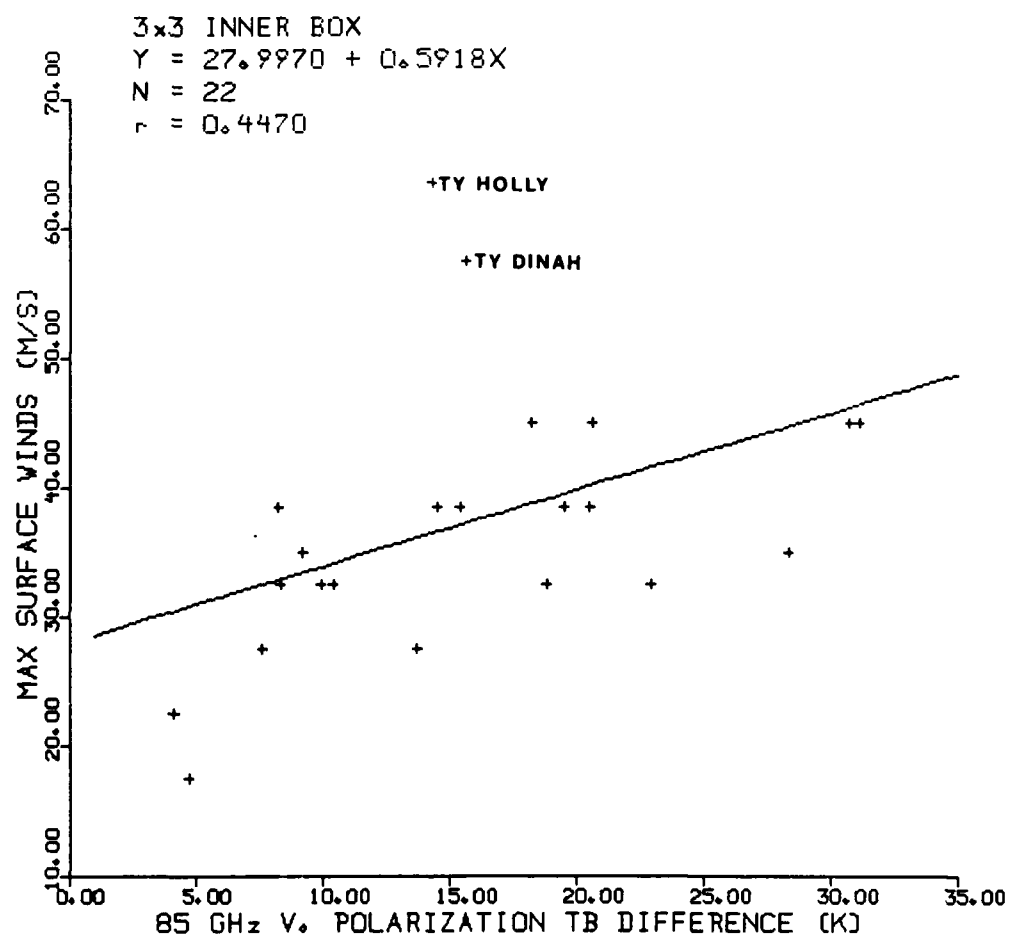


Figure 6.7. Scatter plot of tropical cyclone maximum wind speeds versus 85 GHz vertically polarized brightness temperature difference for the 3x3 inner box case.

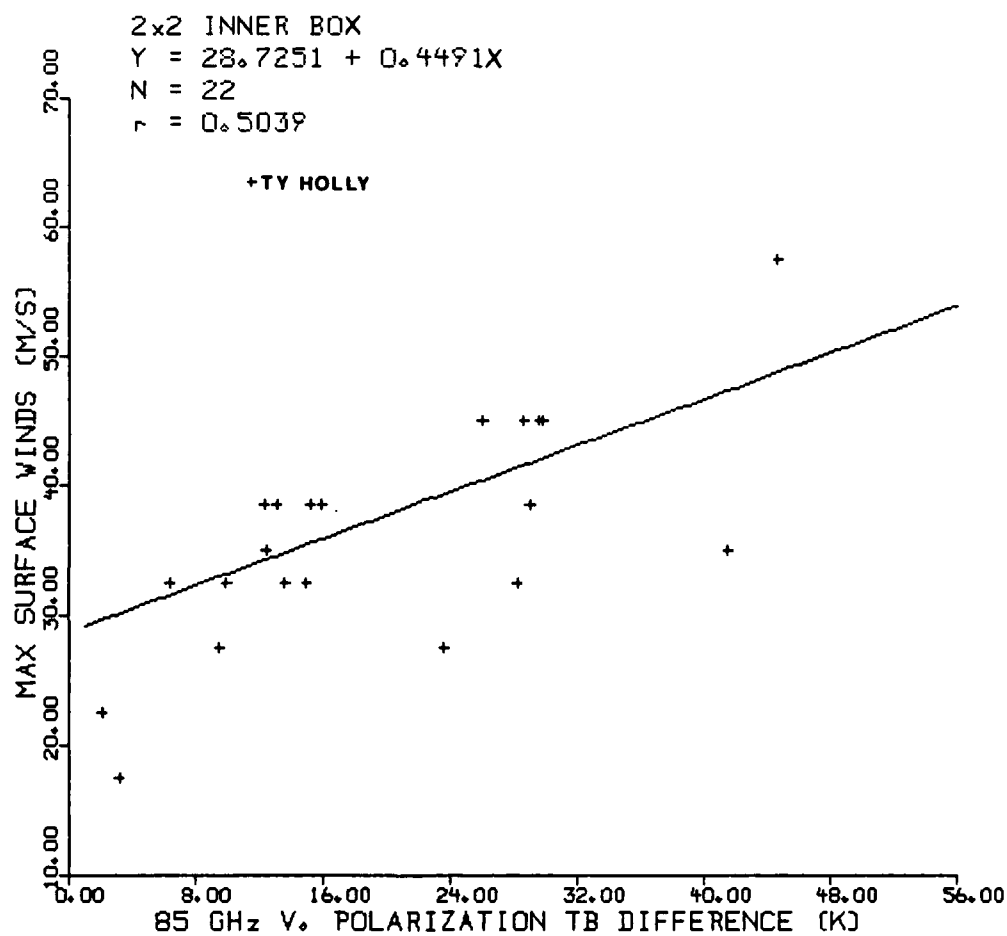


Figure 6.8. As in Fig. 6.7 except for the 2x2° inner box case.

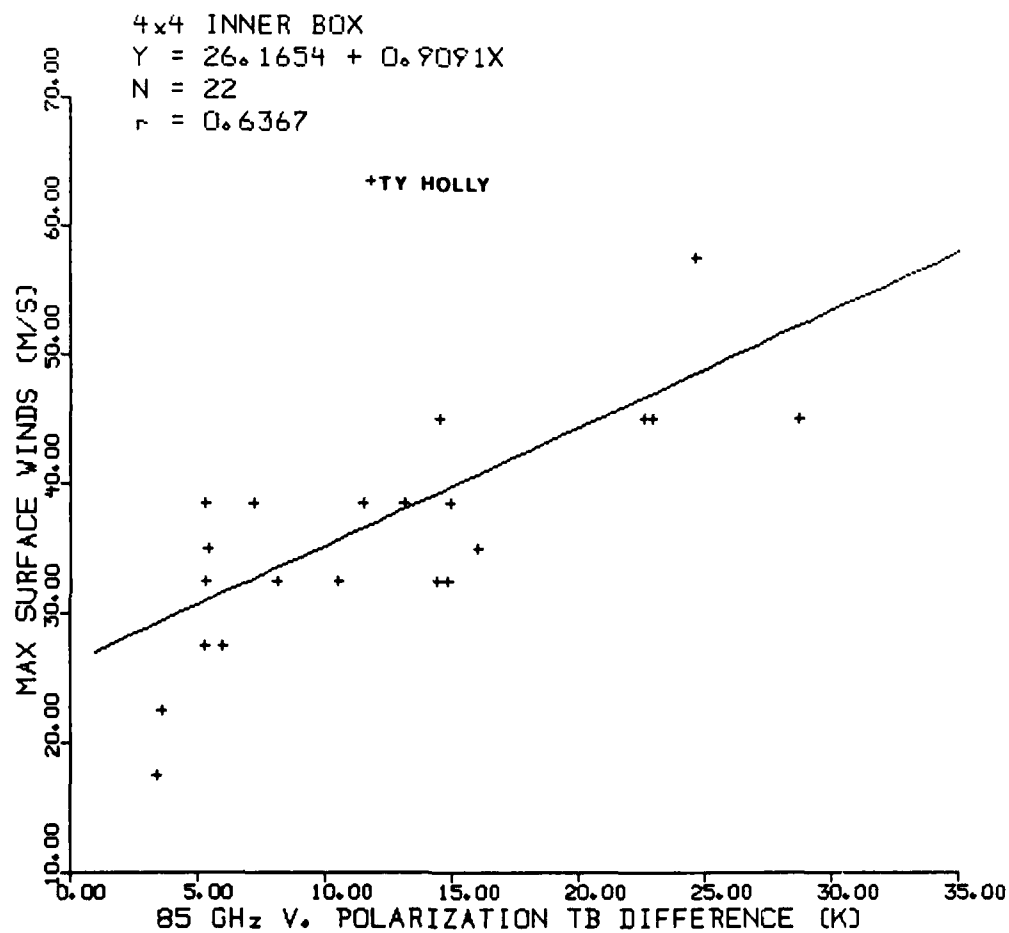


Figure 6.9. As in Fig. 6.7 except for the 4x4° inner box case.

It should be mentioned that the determination of the CI through the use of the Dvorak technique is very subjective. At the same time, the determination of the TB differences between the large and small sized boxes is very precise. Because a subjective value is compared to an exact measurement, this leads to a lower correlation than if both variables were measured in a precise manner.

Earlier it was mentioned that Typhoons Holly and Dinah seemed to be anomalous cyclones. This apparent anomaly can be explained as follows. In reviewing the plotted rain rates used in the LHR calculations, it was noted that Typhoon Holly did develop two unique characteristics which set it apart from other cyclones whose wind speeds were in excess of 40 m s^{-1} . For Typhoon Holly the average rain rate for the area of 111 km radius was smaller than the corresponding rate for the area of 222 km radius. Another unique characteristic was its low PIP value of 0.08. This value was much less than the second lowest cyclone (Typhoon Wynne) which had a value of 0.21. The rest of the cyclones had PIP values greater than 0.25.

How does this relate to the anomalous TB differences? In mature cyclones, the largest rain rates usually occur near the eyewall and inner rainbands where the strongest convection exists. This will result in very low observed 85 GHz TB's. But in Typhoon Holly, its low PIP indicates it consisted of a lower, more uniform rain rate with most of the rain rates being less than 6 mm hr^{-1} . This will result in a more uniform 85 GHz TB over the entire cyclone.

Another important observation is that at the time of the SSM/I pass (9 Sept 1987 @ 0810 UTC) Typhoon Holly was within six hours of reaching its maximum intensity of 140 kts (70 m s^{-1}). Rodgers and Adler (1981) showed LHR values decrease one to two days before the maximum cyclone intensity is reached. This infers that the total storm rainfall also decreases. Fig. 6.1 showed a one to two day lag in TB's measured near the core of the cyclone (region of maximum convection) and the maximum cyclone intensity. This is what has occurred to Holly. It was near its maximum intensity, but the convection and associated heavy rain rates in its eyewall and inner rainbands had already begun to weaken 1-2 days prior to the SSM/I pass. This leads to a more uniform, weakening rain

rate over the entire cyclone (as noted by a low PIP), and therefore a more uniform 85 GHz TB.

Typhoon Dinah also stood out in the $3 \times 3^\circ$ case for the same reason. At the time of the SSM/I pass (25 Aug 1987 @ 0935 UTC) Dinah was less than 12 hours away from its maximum intensity of 137 kts (63.5 m s^{-1}). It therefore had the same uniform 85 GHz TB field as Typhoon Holly.

It should be noted that 22 cyclones were used in this study as compared to 23 cyclones used in the LHR study (Table 4.1). Typhoon Freda (11 Sept 87 @ 0930 UTC) was discarded because it showed a negative TB difference between the inner radii of the storm and its surroundings. It fits the same scenario as Typhoon Holly. It reached maximum intensity approximately 18 hours before the SSM/I pass.

c. 85 GHz TB'S as a forecasting parameter of cyclone intensity

As mentioned earlier, Gentry et al. (1980) found a stronger correlation between the TBB's and the future intensity of the cyclone rather than between TBB's and the current intensity. In this section a similar experiment using the SSM/I data is made.

Using the same TB differences obtained in the previous section for the $2 \times 2^\circ$, $3 \times 3^\circ$, and $4 \times 4^\circ$ boxes, these values are compared to the winds 24 hours after the SSM/I pass. The maximum wind speeds at the 24 point were obtained from the data provided by JTWC which gave the CI. The scatter diagrams for the 24 hour forecast are shown in Figs. 6-10 through 6-12. The t-distribution test showed all three cases to be significant at the 1% level or less.

It is seen that only 20 cases were used in the forecast study in contrast to the 22 used in the previous test. The reason for this is that the two cases which were omitted involved Hurricane Florence, which made landfall in the 24 hours after each of the two time periods used previously. Since making landfall changes the structure of a cyclone, Florence was therefore unique in comparison to the rest of the cyclones and was not included.

The results show that a stronger correlation exists between the TB differences and the forecasted cyclone intensity at the 24 hour point. This holds true for all three of the different sized inner boxes. If the data for Typhoons Holly

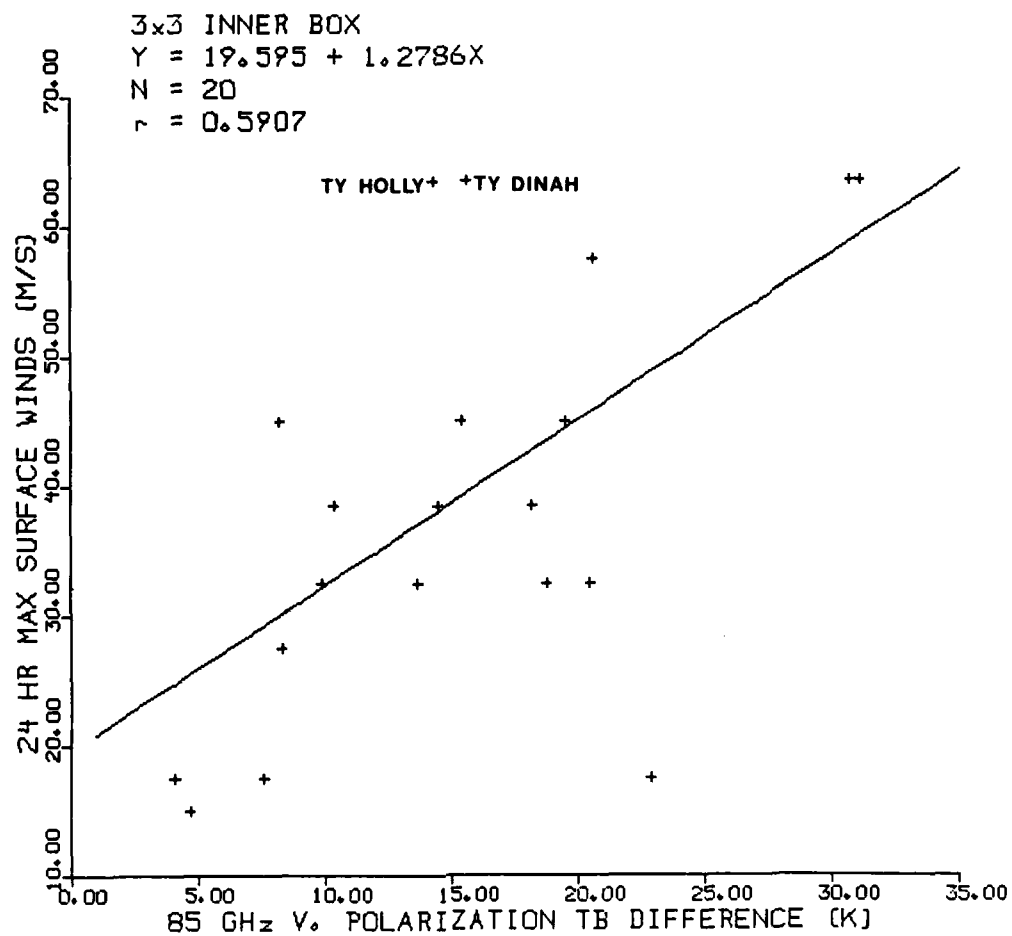


Figure 6.10. Scatter plot of 24 hour cyclone maximum wind speeds versus 85 GHz vertically polarized brightness temperature difference for the 3x3° inner box case.

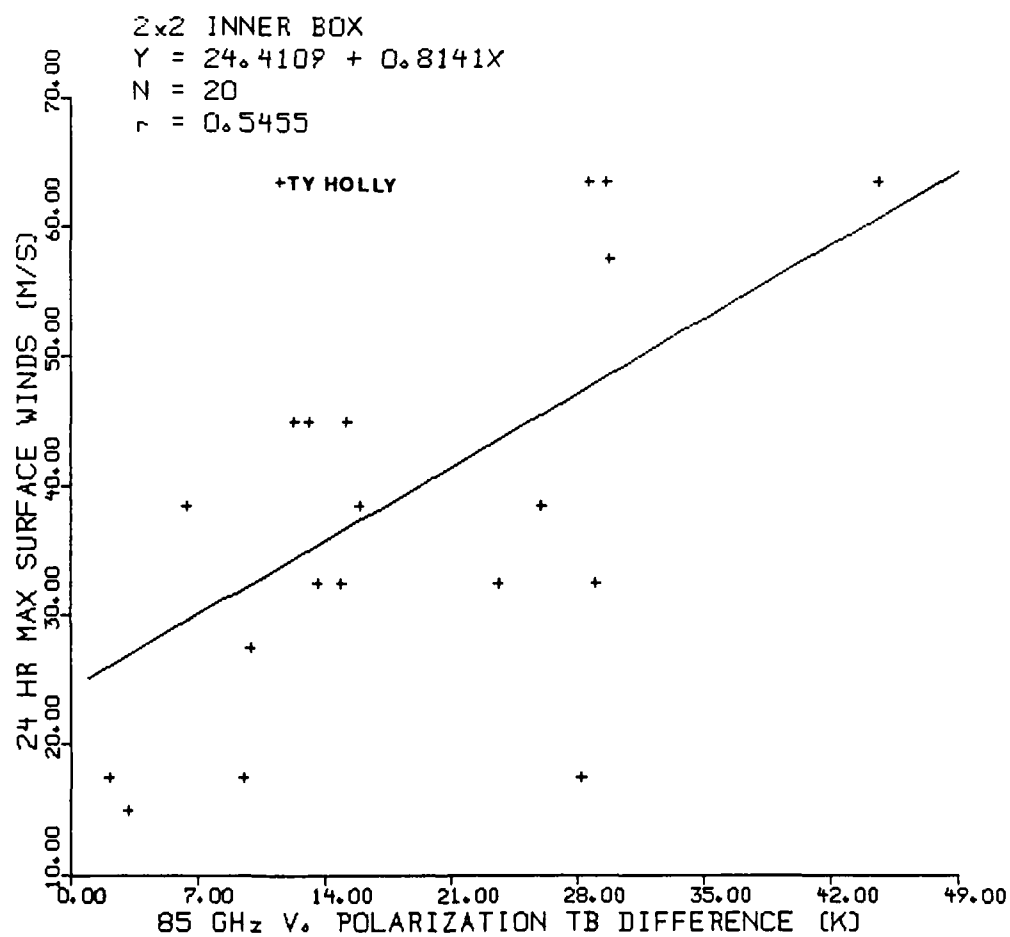


Figure 6.11. As in Fig. 6.10 except for the 2x2^o inner box case.

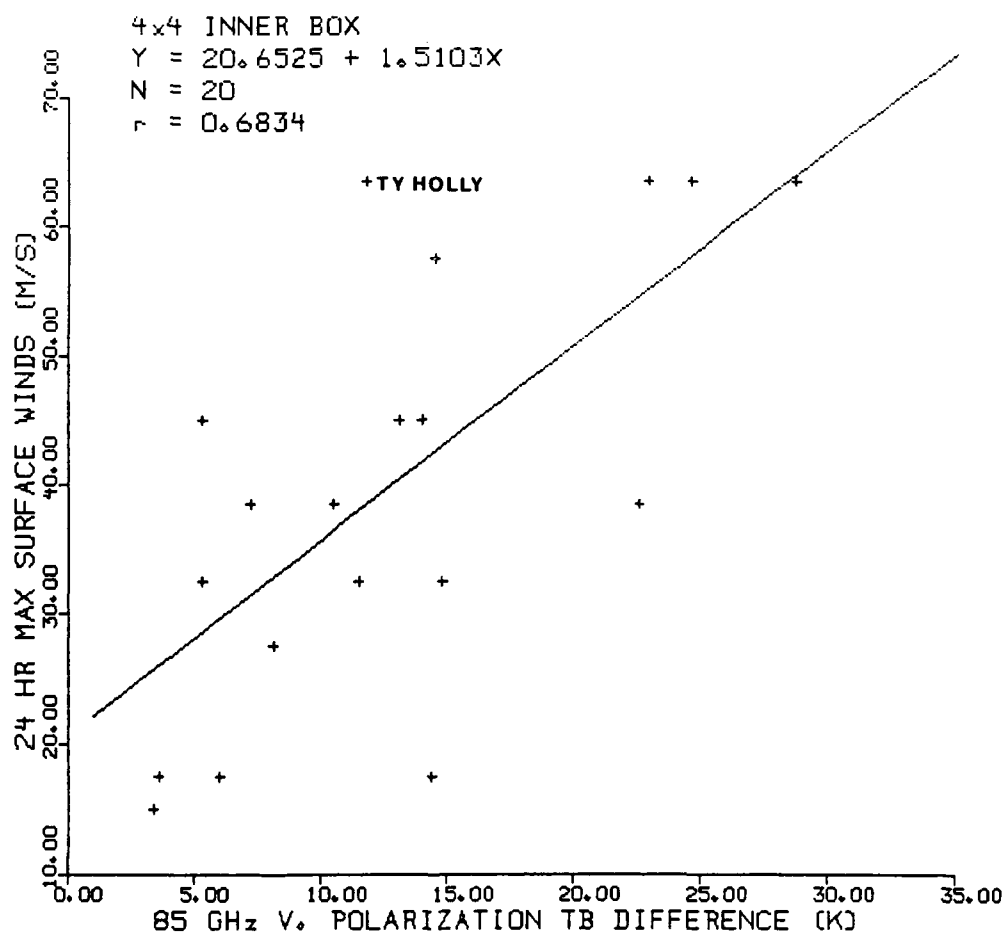


Figure 6.12. As in Fig. 6.10 except for the 4x4° inner box case.

and Dinah are once again removed, as was done in the previous section, the results show improvement. The correlations rose to 0.64, 0.70, and 0.74 for the $2 \times 2^\circ$, $3 \times 3^\circ$, and $4 \times 4^\circ$ sized inner boxes, respectively.

Although the sample size of this study is rather small (20-22 cases), the results show that the TB data from the vertically polarized 85 GHz channel can be useful in determining both the cyclones' current intensity as well as its future (24 hour) intensity.

d. Detection of a tropical cyclone eye

Of the 20 SSM/I passes used in the previous study, there were three cyclones having a visible eye as seen by visual/infrared satellite data. Typhoon Dinah (25 Aug 1987 @ 0935 UTC SSM/I pass) was reported to have a 24 nm (39 km) eye, Typhoon Holly (9 Sept 1987 @ 0810 UTC) had a 20 nm (32 km) diameter eye, and Typhoon Wynne (25 Jul 1987 @ 2020 UTC) with a 16 nm (26 km) eye. Due to the superior footprint resolution (15×13 km) and a scan spacing of only 12.5 km between pixels, it seems reasonable to expect the 85 GHz channel to have the ability to detect an eye the size of those listed above.

Due to the strong subsidence in the eye there will be little if any convection present. With a lack of convection, the amount of ice hydrometeors present in the eye region should be very small. It is possible though, for a thin layer of cirrus, from nearby convection, to cover the eye. The lack of any significant amount of ice hydrometeors should lead to very little scattering of microwave radiation at 85 GHz. Because of the lack of scattering, the observed 85 GHz TB should be warmer in the eye region than it will be for the area surrounding the eye, which consists of the heavy convection associated with the eyewall. So it seems reasonable to expect well defined eyes to show up as warm regions in the 85 GHz TB data. To verify if this holds true, north-south and west-east cross sections of the 85 GHz TB's were analyzed for each of the three cyclones which had visible eyes.

Figs. 6.13 and 6.14 show Typhoon Dinah, which had the largest reported eye at 39 km in width. Both cross sections show warm TB's (250-275° K) at or near the cyclone center. The low TB's on each side of the eye indicate the eyewall and its associated strong convection. The lowest TB's are to the south (130°K) and east (172°K) of the eye.

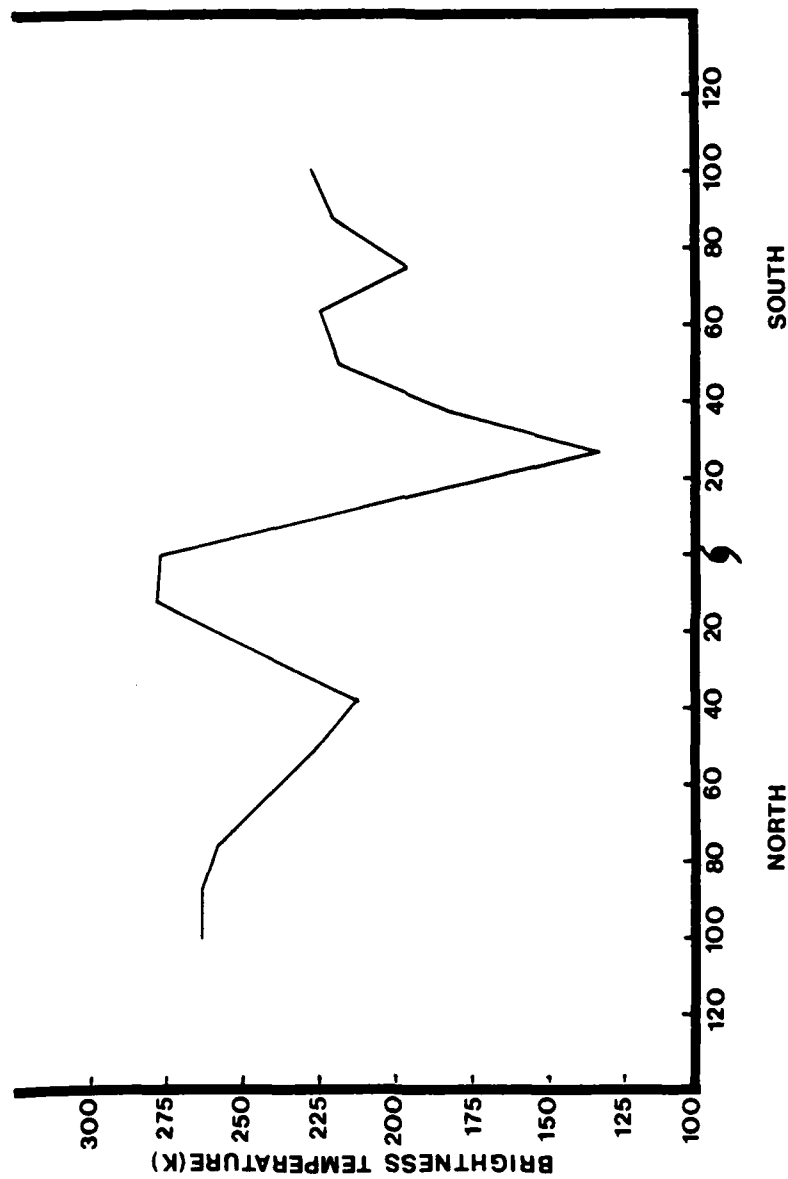


Figure 6.13. North-south cross section of TB's for Typhoon Dinah. Distance in Km from the center of the cyclone are depicted on the x-axis.

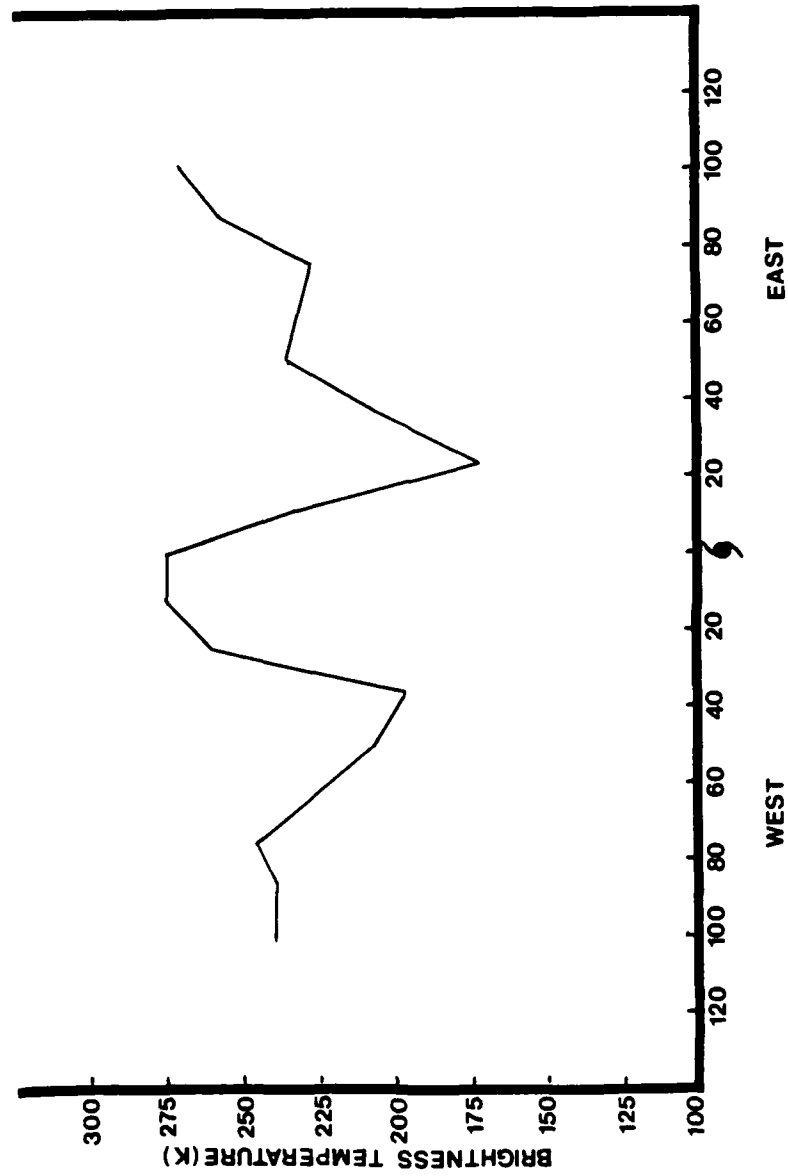


Figure 6.14. As in Fig. 6.13 except this is a west-east cross section.

In fact, the rain rates for Typhoon Dinah showed that in the region surrounding the cyclone center, the largest values were just south (12 mm hr^{-1}) and east (9 mm hr^{-1}) of the center. The smallest rain rates were to the north and west at 4 and 6 mm hr^{-1} , respectively. The size of the eye on the TB cross sections is comparable to the 39 km reported by JTWC.

Figs. 6.15 and 6.16 show the cross sections for Typhoon Holly. Once again the eye is characterized by an area of warm TB's. The spike of warm TB's is smaller than it was for Typhoon Dinah. This is reasonable because the size of the eye reported by JTWC was smaller (32 km). Convection in the eyewall showed up as colder ($\approx 200^\circ\text{K}$) TB's. Typhoon Wynne (Figs. 6.17 and 6.18) had the smallest eye at 26 km. The plot of TB's reveals a double maximum. The larger, more pronounced temperature maximum occurs at the cyclone center, while a smaller maximum occurs 25-35 km to the south and east of the cyclone center.

The cross sections of TB's for the three cyclones show that the 85 GHz TB data can be used to locate the eye. Many times an eye may be present but covered up by a thin layer of cirrus.

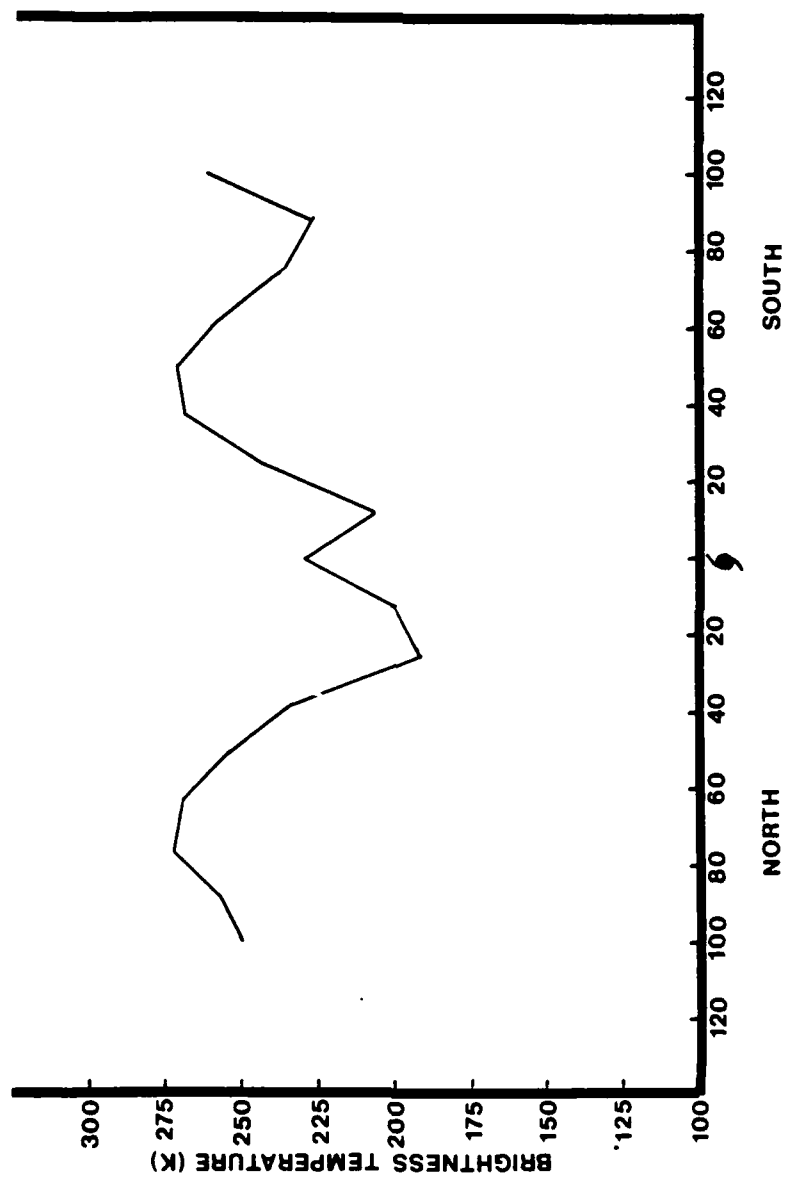


Figure 6.15. As in Fig. 6.13 except for Typhoon Holly.

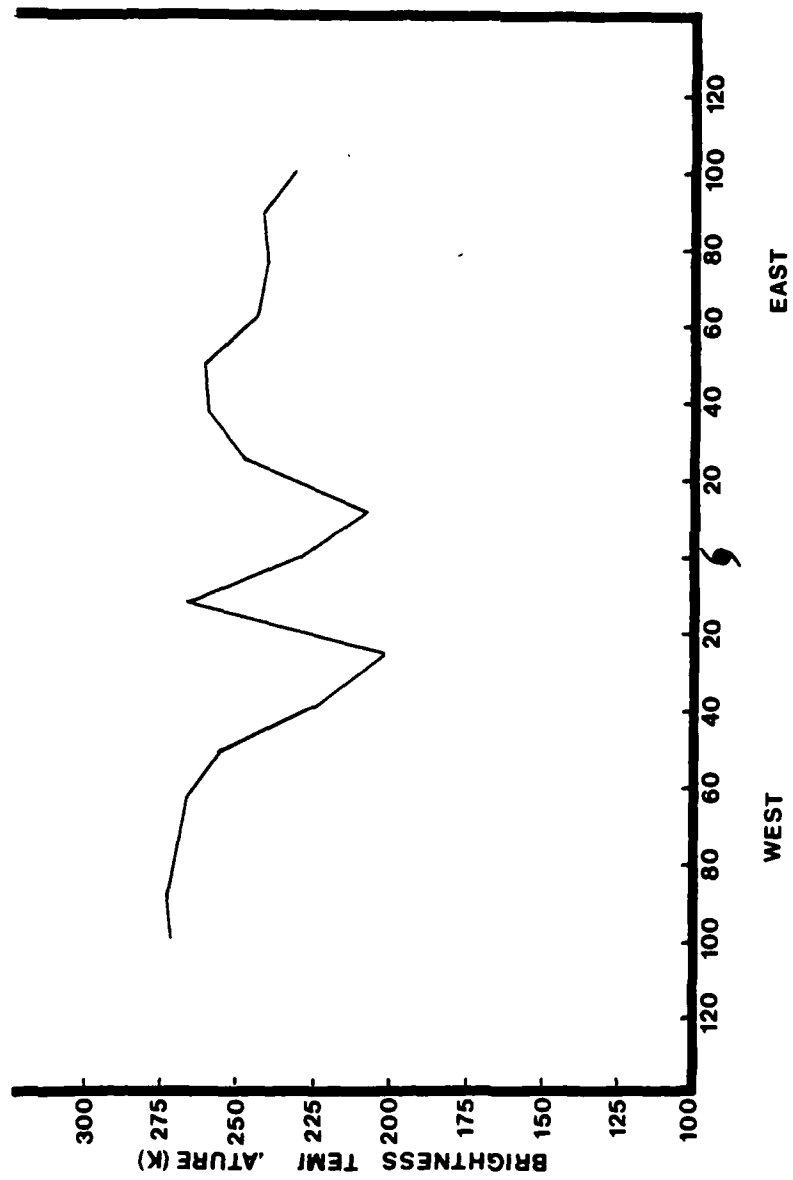


Figure 6.16. As in Fig. 6.14 except for Typhoon Holly.

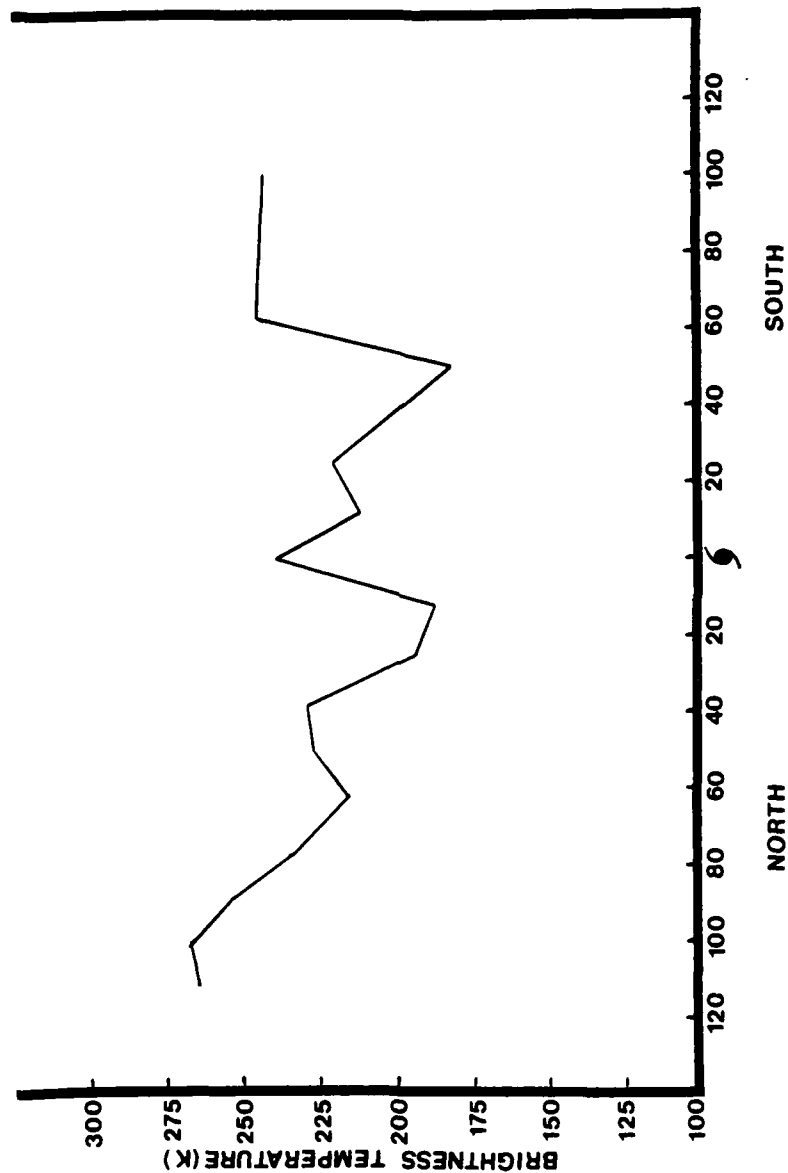


Figure 6.17. As in Fig. 6.13 except for Typhoon Wynne.

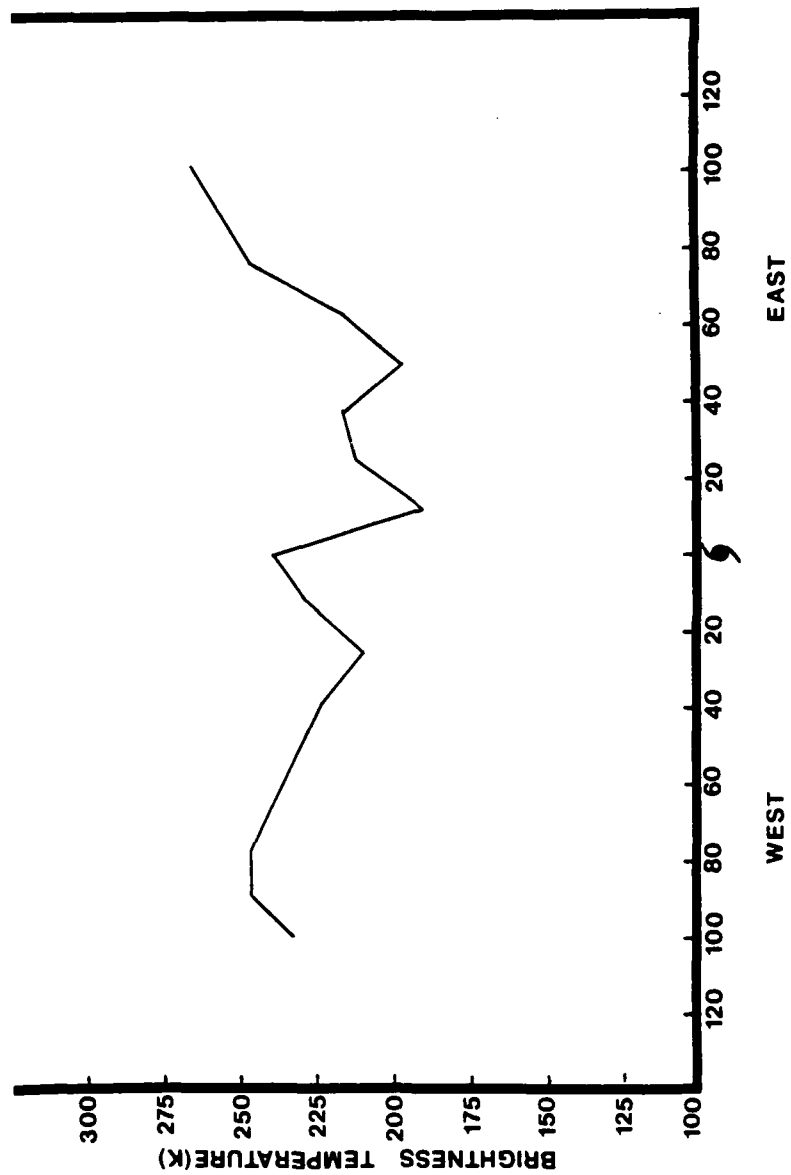


Figure 6.18. As in Fig. 6.14 except for Typhoon Wynne.

As was seen, if the layer of cirrus is thin, the TB data at 85 GHz should show a warm region under this cirrus.

7. CONCLUSIONS

This study has shown that the SSM/I provides valuable data to determine the current intensity of tropical cyclones, as well as a 24 hour forecast of intensity.

In order to correctly apply the data an understanding of the radiative transfer processes at the SSM/I frequencies is essential. It was shown that the absorbing coefficient for raindrops is at a maximum at lower rain rates, while the scattering becomes important above a critical rain rate. It was also seen how this scattering is frequency dependent. Above this critical rain rate the TB's will actually decrease as the rain rate continues to increase. It was also shown that at the high frequencies (37 and 85.5 GHz), the scattering due to ice hydrometeors is very important.

Since this study was only concerned with radiometric measurements of tropical cyclones over oceanic regions, it was shown that changes in wind speeds over the surface of the ocean leads to an increase in the measured TB. Rain will also cause an increase in the surface emission and therefore can lead to an increase in the measured TB. This

causes a problem, especially when surface wind speeds are measured in the presence of rain. At low wind speeds, the rain caused the SSM/I to greatly over estimate the wind speeds.

The SSM/I derived rain rates are useful in estimating the LHR associated with tropical cyclones. The LHR calculated at various radii were shown to be comparable to previous estimates. A strong correlation was found between the calculated LHR and the current intensity for each tropical cyclone. The ability to see the rainband structure using the SSM/I data and its associated asymmetry, is an advantage over the visible and infrared satellite data.

Besides using derived SSM/I parameters such as wind speeds and rain rates, the actual TB data were found to be useful. The 85 GHz vertically polarized TB data were used to compare the average TB for an inner box surrounding the core region of the cyclone, to the average TB for an outer box which consisted mainly of the environment of the tropical cyclone. A strong correlation was found between the difference in the TB's of these two boxes and the intensity of the cyclone. A stronger correlation exists between this TB

difference and the 24 hour intensity of the cyclone.

It was shown that the 85 GHz TB's can be useful in locating the eye of a tropical cyclone. This will facilitate an accurate positioning of the cyclone.

While the SSM/I data are helpful, there are certain drawbacks. First, the field of view (approximately 800 km^2) leads to an averaging of the data. The idea of trying to compare wind speeds for an area of this size to an in situ measurement is obviously flawed. Unfortunately, the only way to minimize this problem is to set a temporal criteria such that the SSM/I pass is as close in time as possible to the in situ wind measurement. Secondly, our inability to more accurately specify such parameters as the concentration and distribution of precipitating particles (liquid and ice hydrometeors), height of the freezing level, thickness of the ice layer, and amount of non-precipitating liquid water can all lead to errors in the model radiative transfer calculations. This will result in errors in the derived TB's.

Despite these drawbacks, the SSM/I presented us with some unique views of tropical cyclones *

unattainable with conventional satellite data
using only visible and infrared frequencies.

REFERENCES

- Adler, R.F., and E.B. Rodgers, 1977: Satellite-observed latent heat release in a tropical cyclone. Mon. Wea. Rev., 105, 956-963.
- Allison, L.J., E.B. Rodgers, T.T. Wilheit, and R.W. Fett, 1974: Tropical cyclone rainfall as measured by the Nimbus-5 Electrically Scanning Microwave Radiometer. Bull. Amer. Meteor. Soc., 55, 1074-1089.
- Barrett, E.C., and D. Martin, 1981: The Use of Satellite Data in Rainfall Monitoring. Academic Press, 124-171 pp.
- Black, P.G., R.C. Gentry, V.J. Cardone, and J.D. Hawkins, 1985: Satellite Microwave Wind and Rain Observations in Severe Tropical and Mid-latitude Marine Storms. Advances in Geophysics, Vol 27. Satellite Remote Sensing. Ed. by Barry Saltzman. Academic Press, 197-277 pp.
- Droppleman, J.D., 1970: Apparent microwave emissivity of sea foam. J. Geophys. Res., 75, 696-697.
- Dvorak, V.F., 1984: Tropical cyclone analysis using satellite data. NOAA Tech Report NESDIS 11, US Dept of Commerce, 47 pp.
- Elsberry, R.L., W.M. Frank, G.J. Holland, J.D. Jarrell, and R.L. Southern, 1985: A Global View of Tropical Cyclones. Extended abstracts from the International Workshop on Tropical Cyclones, 28 November - 5 December 1985, Bangkok, Thailand, 185 pp.
- Gentry, R.C., E.B. Rodgers, J. Steranka, and W.E. Shenk, 1980: Predicting tropical cyclone intensity using satellite-measured equivalent blackbody temperatures of cloud tops. Mon. Wea. Rev., 108, 445-455.
- Hawkins, J.D., and P.G. Black, 1983: SEASAT scatterometer detection of gale force winds near tropical cyclones. J. Geophys. Res., 88, 1674-1682.

Hollinger, J.T., R. Lo, G. Poe, R. Savage, and J. Peirce, 1987: Special Sensor Microwave/Imager (SSM/I) User's Guide, Dept of the Navy, Naval Research Lab., Wash. D.C., 120 pp.

Hsu, S.A., 1981: Models for estimating offshore winds from onshore meteorological measurements. Boundary-Layer Meteor., 20, 341-351.

Hunter, H.E., E.B. Rodgers, and W.E. Shenk, 1981: An objective method for forecasting tropical cyclone intensity using Nimbus-5 Electrically Scanning Microwave Radiometer measurements. J. Appl. Meteor., 20, 137-145.

Jorgensen, D.P., and P.T. Willis, 1982: A Z-R relationship for Hurricanes, J. Appl. Meteor., 21, 356-366.

Kidder, S.Q., W.M. Gray, and T.H. Vonder Harr, 1978: Estimating tropical cyclone central pressure and outer winds from satellite microwave data. Mon. Wea. Rev., 114, 1539-1546.

Liou, K.N., 1980: An Introduction to Atmospheric Radiation. Academic Press, 392 pp.

Lovejoy, S., and G.L. Austin, 1980: The estimation of rain from satellite-borne microwave radiometers. Quart. J. Roy. Meteor. Soc., 106, 255-276.

Marks, F.D., 1985: Evolution of the structure of precipitation in Hurricane Allen (1980). Mon. Wea. Rev., 113, 909-931.

Norberg, W., J. Conaway, D.B. Ross, and T.T. Wilheit, 1971: Measurements of microwave emissions from a foam-covered, wind-driven sea. J. Ats. Sci., 28, 429-435.

Olson, W.S., 1987: Estimation of Rainfall Rates in Tropical Cyclones by Passive Microwave Radiometry. PhD. Dissertation, 282 pp.

Parrish, J.R., R.W. Burpee, and F.D. Marks, 1982: Rainfall patterns observed by digitized radar during landfall of Hurricane Frederic (1979). Mon. Wea. Rev., 110, 1933-1944.

Rao, M.S., 1984: Retrieval of Worldwide Precipitation and Allied Parameters from Satellite Microwave Observations. Advances in Geophysics, Vol 26, Ed. by Barry Saltzman. Academic Press, 237-336 pp.

Riehl, H., 1979: Climate and Weather in the Tropics. Academic Press, 611 pp.

Rodgers, E.B., and R.F. Adler, 1981: Tropical cyclone rainfall characteristics as determined from a satellite passive microwave radiometer. Mon. Wea. Rev., 109, 506-521.

Spencer, R.W., B.B. Hinton, and W.S. Olson, 1983: Nimbus-7 37GHz radiances correlated with radar rain rates over the Gulf of Mexico. J. Climate and Appl. Meteor., 22, 2095-2099.

-----, 1986: A satellite passive 37GHz scattering-based method for measuring oceanic rain rates. J. Climate and Appl. Meteor., 25, 754-766.

Staff, Joint Typhoon Warning Center, 1987: Annual Tropical Cyclone Report. NAVOCEANCOMCEN/JTWC, 213 pp.

Steranka, J., E.B. Rodgers, and R.C. Gentry, 1986: The relationship between satellite measured convective bursts and tropical cyclone intensification. Mon. Wea. Rev., 114, 1539-1546.

Ulaby, F.T., R.K. Moore, and A.K. Fury, 1981: Microwave Remote Sensing, Active and Passive. Vol 1. Microwave Remote Sensing. Fundamentals and Radiometry. Addison-Wesley Publishing Co, 456 pp.

Weatherford, C.L., and W.M. Gray, 1985: Typhoon Structure Variability. Dept. of Atmospheric Science Paper No. 391, Colorado State University, 77 pp.

Webster, W.W., T.T. Wilheit, D.B. Ross, and P. Gloersen, 1976: Spectral characteristics of the microwave emission from a wind-driven foam-covered sea. J. Geophys. Res., 81, 3095-3099.

Wilheit, T.T., A.T. Chang, M.S.V. Rao, E.B. Rodgers, and J.S. Theon, 1977: A satellite technique for quantitatively mapping rainfall rates over the oceans. J. Appl. Meteor., 16, 551-560.

-----, 1979: The effects of wind on the microwave emission from the ocean's surface at 37GHz. J. Geophys. Res., 84, 4921-4926.

-----, A.T. Chang, J.L. King, and E.B. Rodgers, 1982: Microwave radiometric observations near 19.35, 92 and 183 GHz of precipitation in Tropical Storm Cora. J. Appl. Meteor., 21, 1137-1145.

Wu, R., and J.A. Weinman, 1984: Microwave radiances from precipitating clouds containing aspherical ice, combined phase, and liquid hydrometeors. J. Geophys. Res., 89, 7170-7178.

BIOGRAPHY

Don Kenneth Rhudy [REDACTED]

[REDACTED] a. He graduated from Mead High School in Spokane, Washington in 1975. After attending two years at a local Community College, he attended Oregon State University majoring in Atmospheric Sciences. Upon graduation in June 1980 he joined the United States Air Force and was commissioned on February 27, 1981. He then spent three years as a Wing Weather Officer to the 436th Military Airlift Wing at Dover, Delaware. In April 1984 he left for Osan Air Base, Republic of Korea, where he worked as the Meteorological Satellite Coordinator and was responsible for all DMSP data used by U.S. Forces in Korea. Upon returning the U.S. in June 1985 the author was assigned to HQ Air Weather Service where he worked until his selection to attend graduate school at St. Louis University in August 1987. The author is married to the former Martha Joy Woods.